Materials Advances

Accepted Manuscript

This article can be cited before page numbers have been issued, to do this please use: Z. Y. Khattari and Y. N. Zhuravlev, *Mater. Adv.*, 2026, DOI: 10.1039/D6MA00450D.

ROYAL SOCIETY OF CHEMISTRY

rsc.li/materials-advances

View Article Online
DOI: 10.1039/D6MA00450D

High-Pressure Behavior of $MgAgF_3$ Perovskite: Structural Anisotropy, Pressure-Induced Structural Evolution, and Band Gap Tuning

Z.Y. Khattari[1*], Yu. N. Zhuravlev[2]
[1] Department of Physics, Faculty of Science, The Hashemite University, P. O. Box 330127, Zarqa 13133, Jordan

[2] Institute of Fundamental Sciences, Kemerovo State University, Krasnaya 6, 650000, Kemerovo, Russia

[*]Corresponding author: zkhattari@hu.edu.jo (Z.Y. Khattari)

Abstract

The pressure-dependent structural and electronic properties of the hexagonal perovskite $MgAgF_3$ have been systematically investigated using first-principles density functional theory calculations within the CASTEP code, covering a pressure range of 0–50 GPa. The ambient crystal structure (space group $R3c$, a = b = 5.515 Å, c = 13.549 Å) exhibits a complex structural evolution under compression, with several distinguishable pressure regimes identified from simulated X-ray diffraction patterns and lattice parameter evolution. The material exhibits significant mechanical anisotropy, with the c-axis being more compressible ($B_{0,c}$ = 185.5 GPa) than the a-axis ($B_{0,a}$ = 280.6 GPa), resulting in a 22.2% unit cell volume reduction over 50 GPa. Bond analysis reveals that F—Mg bonds become increasingly covalent under pressure (overlap population 0.18 → 0.19), while F—Ag bonds transition from weak covalent to antibonding interactions (0.05 → -0.02). The band gap increases linearly with pressure following $E_g = 2.137 + 0.00667 \times P$ (eV), widening from 2.137 eV at ambient pressure to 2.469 eV at 50 GPa (Δ = +15.5%), with no discontinuities at the pressure regimes identified from the XRD analysis. Notably, induced d-states emerge in Mg between −1 and 0 eV under pressure, consistent with pressure-induced hybridization and enhanced Mg—F covalency. These findings provide a comprehensive pressure-dependent characterization for $MgAgF_3$, suggesting that this lead-free perovskite may be of interests for optoelectronic applications in the visible to near-UV range, with pressure-tunable electronic properties that could potentially be explored for strain-engineered devices.

Keywords: Perovskite; Magnesium silver fluoride; High pressure; Density functional theory; Band gap engineering; Anisotropic compression; CASTEP.

View Article Online
DOI: 10.1039/D6MA00450D

1. Introduction

Perovskite-structured compounds have garnered immense scientific and technological interest due to their remarkable physical properties and broad applicability across energy, electronics, and optoelectronics.[1-4] Perovskites are materials with the general formula ABX_3, where A and B are cations of different sizes and X is an anion (typically oxygen or a halogen). In this structure, the B-site cation is coordinated by six X anions forming an octahedron, while the A-site cation occupies a 12-coordinate cavity. While the archetypal perovskites are oxygen-based with the general formula ABO_3, halide analogues—particularly fluoro-perovskites (ABF_3)—have emerged as a fascinating class of materials owing to their mechanically stable crystal structures and good optoelectronic properties.[5-7] Fluorine, being the most electronegative element, forms chemically stable fluorides with low-electro-negativity alkali and alkaline earth metals, making fluoro-perovskites promising candidates for applications ranging from photolithography lenses and UV optical windows to semiconductor fabrication.[8-10]

Fluoro-perovskites exhibit energy band gaps spanning the semiconducting (1–4 eV) to insulating (>4 eV) regimes, positioning them as versatile materials for a wide spectrum of applications.[11-13] Among these, $KMgF_3$ has pointed out promising performance in UV spectral regions, enabling its use in transparent, low-loss optical components.[14, 15] Similarly, compounds such as $NaSrF_3$, $NaBaF_3$, and $LiBaF_3$ have been investigated for their potential in UV photonic systems.[16] Beyond optical applications, fluoride perovskites also display interesting functional properties including piezoelectricity, ferromagnetism, and photoluminescence.[17-19]

The physical properties of fluoride perovskites have been extensively investigated using first-principles methods. Jin et al. studied the pressure-dependent electronic, elastic, optical, and thermodynamic properties of cubic $NaBaF_3$, reporting a direct band gap that increases with pressure and a phase transition at 68.8 GPa.[19] Xu et al. investigated $LiMgF_3$ under pressure up to 30 GPa, finding an indirect band gap of 5.776 eV that widens with pressure, accompanied by blue-shifted optical spectra.[20] Most relevant to the present work, Kocak and Ciftci systematically examined the structural, electronic, mechanical, lattice dynamical, and optical properties of $XMgF_3$ (X = Li, K, Rb) over the 0–50 GPa range, establishing their mechanical stability and insulating character.[21] Khan et al. investigated indium-based fluoroperovskites $InAF_3$ (A = Ca,

View Article Online
DOI: 10.1039/D6MA00450D

Cd, Hg), reporting direct band gaps of 3.66 eV and 3.29 eV for $InCaF_3$ and $InCdF_3$, respectively, with ductile and anisotropic mechanical behavior.[22] Szeleszczuk et al. explored the optoelectronic and thermoelectric performance of double perovskites X_2YInO_6 (X = Ba, Sr; Y = Nb, V), highlighting their potential for high-temperature applications.[23] These studies provide important context for understanding the high-pressure behavior of Ag-based fluoroperovskites such as $MgAgF_3$.

Recent years have witnessed significant advances in the computational exploration of fluoro-perovskites, with density functional theory (DFT) providing valuable insights into their structural, electronic, and optical characteristics.[24-26] Siddiqua et al. recently conducted a comprehensive DFT study of rhombohedral $MgAgF_3$, reporting an indirect band gap of 2.16 eV, mixed ionic-covalent bonding, mechanical stability with ductile behavior (Pugh's ratio = 2.14), and significant UV absorption.[24] This study laid foundational insights into $MgAgF_3$ crystals potential for optoelectronic applications, particularly in UV photonic systems and polarized light detectors.

More recently, Fatima et al. performed first-principles calculations on the cubic phase of $AgYF_3$ (Y = Mg, Sr) using the full-potential linearized augmented plane wave (FP-LAPW) method implemented in Wien2k.[25,26] Their study employed multiple exchange-correlation functionals—Perdew–Burke–Ernzerhof of Generalized Gradient Approximation of (PBE-GGA) and PBEsol potentials[27], The Trans–Blaha modified Becke–Johnson (TB-mBJ)[28], and SCAN[29]—to accurately probe the structural, electronic, and optical properties of these lead-free halide perovskites. They reported optimized lattice constants of 3.923 Å (PBEsol) and 3.991 Å (PBE-GGA) for $AgMgF_3$, in good agreement with experimental values of 3.920 Å.[30,31] The electronic band gap of $AgMgF_3$ was calculated as 1.96 eV (PBEsol), 5.25 eV (TB-mBJ), and 2.59 eV (SCAN), all exhibiting an indirect M–Γ band gap nature.[25] Notably, they observed that $AgSrF_3$ transitions from an indirect to a direct band gap when calculated with the SCAN functional, highlighting the importance of using advanced meta-GGA functionals for accurate electronic structure predictions. Their comprehensive optical analysis revealed strong absorption peaks in the ultraviolet energy region, low reflectivity, and high optical conductivity for both perovskites, advocating their utility in solar technology and optoelectronic devices.[25,30,31] Yu et al.

View Article Online
DOI: 10.1039/D6MA00450D

investigated the structural, elastic, electronic, and optical properties of cubic $AgXF_3$ (X = Be, Mg, Ca, Sr) using the PBEsol functional, reporting an indirect band gap of 1.901 eV and a bulk modulus of 85.64 GPa for $AgMgF_3$.[32] Reshak et al. explored the pressure-induced physical variations in lead-free fluoro-perovskites XYF_3 (X = K, Rb, Ag; Y = Zn, Sr, Mg), reporting systematic band gap increases with pressure and shifts in optical absorption edges.[33] Essaoud et al. characterized the structural, dynamic, optoelectronic, thermodynamic, mechanical, and thermoelectric properties of $AMgF_3$ (A = K, Ag), reporting a band gap of 5.246 eV for $AgMgF_3$ using TB-mBJ and a high figure of merit for thermoelectric applications.[34] Ahmed et al. computed the elastic properties of ABF_3 (A = Ag, K; B = Mg, Zn) using Quantum ESPRESSO, reporting a bulk modulus of 80.10 GPa for $AgMgF_3$.[35] Murtaza et al. earlier studied cubic $AgTF_3$ (T = Mg, Zn) using Wien2k, reporting a lattice constant of 3.885 Å and a band gap of 0.78 eV for $AgMgF_3$ with the Wu–Cohen functional.[36]

Despite these advances, the high-pressure behavior of $MgAgF_3$ remains largely unexplored. Pressure is a fundamental thermodynamic variable that can induce dramatic changes in crystal structure, bonding, and electronic properties, often revealing new phases and enabling band gap engineering.[37,38] Understanding the pressure-dependent structural evolution and electronic response of $MgAgF_3$ is crucial for assessing its stability under extreme conditions and for exploiting strain engineering in thin-film devices. High-pressure studies on related fluoro-perovskites have revealed interesting phenomena, including pressure-induced phase transitions and band gap modifications. [39-42] For instance, High-throughput computational studies have further expanded the understanding of inorganic halide perovskites. Alqahtani et al. systematically investigated 168 compounds of the form ABX_3 (A = Li, Na, K, Rb, Cs, Tl; B = Be, Mg, Ca, Ge, Sr, Sn, Pb; X = F, Cl, Br, I), identifying 118 highly stable phases and providing a valuable resource for materials discovery. [39] Beyond Mg-based compounds, Hiadsi et al. investigated the structural, electronic, and thermal properties of the zinc-based fluoro-perovskites $AgZnF_3$ and $KZnF_3$ using the FP-(L)APW+lo method with PBE, PBEsol, and TB-mBJ functionals.[40] They reported indirect band gaps for both compounds and confirmed the predominantly ionic character of the metal–fluorine bonds through Quantum Theory of Atoms in Molecules (QTAIM) analysis, findings that are consistent with the bonding behavior observed in this study of $MgAgF_3$ under pressure.[40] Notably, $MgAgF_3$ was not included in that survey,

View Article Online
DOI: 10.1039/D6MA00450D

underscoring the novelty and importance of the present focused investigation. For instance, Rehman et al. recently investigated the pressure-induced modulation of structural, electronic, and optical properties of $LiCaF_3$ for optoelectronic applications, reporting systematic changes in band structure and optical response.[41]

In this work, we present a comprehensive first-principles DFT investigation of the structural and electronic properties of $MgAgF_3$ under hydrostatic pressure from 0 to 50 GPa using the CASTEP code.[32] This study aims to:

1. **Elucidate the pressure-induced structural evolution** of $MgAgF_3$ through simulated XRD patterns and lattice parameter analysis.
2. **Quantify the anisotropic compression behavior** and determine the equation of state and bulk modulus.
3. **Establish the pressure dependence of the electronic band gap** and explore its implications for optoelectronic applications.[42,43]
4. **Map the evolution of the electronic band structure and density of states**, including the emergence of pressure-induced d-states in Mg.
5. **Investigate the pressure-dependent bonding and charge redistribution** using Mulliken and Hirshfeld population analyses.[42,43]
6. **Assess the mechanical and dynamical stability** under compression via elastic constants and phonon dispersion calculations.

By systematically examining the high-pressure behavior of $MgAgF_3$, this work provides critical insights into the structure–property relationships of this lead-free perovskite and offers a theoretical foundation for experimental efforts aimed at synthesizing and engineering $MgAgF_3$-based devices under strain or high-pressure conditions.

2. Materials and Methods

2.1 Computational Details

All DFT calculations were performed using the CASTEP code (version 18.1).[37] The exchange-correlation functional was described by the PBE-GGA.[44] Core-valence interactions were treated

View Article Online
DOI: 10.1039/D6MA00450D

using optimized norm-conserving pseudopotentials generated via the Koelling–Harmon relativistic scheme.[44] The following electronic configurations were used: F ($2s^2 2p^5$), Mg ($2s^2 2p^6 3s^2$), and Ag ($4s^2 4p^6 4d^{10} 5s^1$). Pseudopotential generation was performed with ionic charges of +7 for F, +10 for Mg, and +19 for Ag, ensuring accurate description of the valence electron densities.

2.2 Geometry Optimization

The crystal structure of $MgAgF_3$ was initially taken from data *Materials Project database* data with Material ID: *mp-998418* (space group *R*3*c*, No. 161, a = b = 5.515 Å, c = 13.549 Å, $\alpha = \beta = 90°$, $\gamma = 120°$, V_c = 356.90 $Å^3$, Band Gap = 2.19 eV) under ambient pressure.[44] Full geometry optimizations were performed under hydrostatic pressures ranging from 0 to 50 GPa in increments of 5 GPa (0, 5, 10, 15, 20, 25, 30, 40, and 50 GPa). At each pressure point, both lattice parameters and atomic positions were fully relaxed using the Broyden–Fletcher–Goldfarb–Shanno (BFGS) minimization algorithm.[46] A plane-wave basis set cutoff energy of 570 eV was employed, which was converged with respect to total energy and structural parameters. Brillouin zone sampling was performed using a Monkhorst–Pack grid of 3 × 3 × 1 **k**-points, yielding 5 irreducible **k**-points for the hexagonal cell.[47] Convergence criteria for geometry optimization were set to: energy change < 5.0×10^{-6} eV/atom, maximum force < 0.01 eV/Å, maximum displacement < 5.0×10^{-4} Å, and maximum stress < 0.02 GPa. All calculations were converged within 100 SCF cycles.

2.3 Electronic Properties

Electronic band structures and density of states (DOS) were calculated at the optimized geometries for each pressure point. Band structures were computed along high-symmetry **k**-paths in the hexagonal Brillouin zone (Γ → Z → M → Γ → K → M) using 50 **k**-points per path. Total and partial densities of states (PDOS) were computed using the same **k**-point grid as the

View Article Online
DOI: 10.1039/D6MA00450D

geometry optimization. Partial DOS were analyzed to identify orbital contributions (s, p, d) from each atomic species. Mulliken population analysis[42] and Hirshfeld charge analysis[43] were performed to evaluate charge distribution and bond overlap populations. Charge spilling values were monitored to ensure basis set convergence (spilling < 0.5% for all calculations). To address the well-known band gap underestimation of the PBE-GGA functional, a single-point calculation using the hybrid HSE06 functional (with 25% exact Hartree-Fock exchange) was performed at the optimized geometry at 0 GPa. The HSE06 band gap was used to benchmark the PBE results and to provide a more accurate estimate of the electronic band gap.

2.4 X-ray Diffraction Simulation

X-ray diffraction (XRD) patterns were simulated from the optimized crystal structures using the CASTEP module. Patterns were calculated for Cu K_α radiation (λ = 1.54056 Å) over a 2θ range of 20–45°. Peak positions, *d*-spacings, and relative intensities were extracted for each pressure point. Simulated patterns were normalized to their maximum intensity for visualization.

2.5 Equation of State and Bulk Modulus

The pressure–volume relationship was fitted to the third-order Birch–Murnaghan equation of state[38,48] using the EOS Fit package. The bulk modulus (B_0) and its pressure derivative (B_0') were obtained from the fit. Linear bulk moduli along the a- and c-axes were calculated from the individual lattice parameter compression curves.

2.6. Convergence Tests

Convergence of the total energy with respect to the plane-wave cutoff energy and **k**-point mesh was carefully tested at ambient pressure (0 GPa) using the optimized crystal structure. As shown in Figure S1(a), increasing the cutoff energy from 550 eV to 570 eV changed the total energy by only 0.021 eV, while further increases to 600 eV and 700 eV resulted in changes of less than 0.025 eV. A cutoff energy of 570 eV was therefore selected, providing an optimal balance between accuracy and computational cost.

View Article Online
DOI: 10.1039/D6MA00450D

For the **k**-point mesh (Figure S1(b)), increasing the mesh from 3 × 3 × 1 to 4 × 4 × 1 changed the total energy by only 0.0016 eV, while increasing to 5 × 5 × 1 gave a similar change of 0.0016 eV. The 3 × 3 × 1 mesh was therefore chosen. Since the unit cell volume decreases under pressure, this mesh provides even denser **k**-point sampling at higher pressures, ensuring convergence across the entire 0–50 GPa range.

3. Results

3.1. Crystal Structure

The ambient pressure crystal structure of $MgAgF_3$ was first determined from the well-known Material project database data and is shown in Figure 1.[45] The compound crystallizes in the trigonal space group $R3c$ (No. 161) with lattice parameters a = b = 5.515 Å, c = 13.549 Å, and unit cell volume V = 356.90 Å^3 (Table 1).[45] The structure consists of corner-sharing MgF_6 octahedra, with Mg^{2+} ions in six-fold coordination, while Ag^+ ions occupy nine-coordinate sites. The polyhedral arrangement viewed along the crystallographic c-axis reveals a layered perovskite-type framework, consistent with the hexagonal symmetry and the 6 : 6 : 18 atom distribution ($Z = 6$).[45]

3.2. Computational Validation

To ensure the reliability of this DFT calculations, geometry optimization convergence was carefully monitored. Figure 2 shows the evolution of key convergence criteria during optimization exemplified at 10 GPa. The energy change per atom, maximum atomic displacement, maximum force, and maximum stress all satisfy the convergence thresholds (energy change $< 0.5 \times 10^{-6}$ eV/atom, displacement $< 0.5 \times 10^{-3}$ Å, force < 0.01 eV/Å, stress < 0.02 GPa) within the first 10 optimization steps. Similar convergence behavior was observed at all pressure points, confirming the accuracy and stability of the optimized structures.

The equation of state was determined by fitting the energy-volume data to the third-order Birch–Murnaghan equation. Figure 3 presents the E(V) curves at ambient pressure and 50 GPa, from which the zero-pressure bulk modulus was derived as $B_0 = 81.80$ GPa with pressure derivative $B_0' = 3.90$ (Table 1).[38]

View Article Online
DOI: 10.1039/D6MA00450D

3.3. Pressure-Induced Structural Evolution

3.3.1. Lattice Compression and Anisotropy

The evolution of lattice parameters and unit cell volume under hydrostatic pressure is summarized in Table 1 and illustrated in Figure 4. Both a-, and c-axes decrease monotonically with increasing pressure, with the c-axis showing greater compressibility. Over 50 GPa, the a-axis contracts from 5.515 Å to 5.208 Å (5.6% reduction), while the c-axis contracts from 13.549 Å to 12.090 Å (10.8% reduction), result in a total unit cell volume reduction of 22.2% (from 356.90 Å³ to 277.50 Å³). The linear bulk moduli derived from axial fits reveal significant mechanical anisotropy: $B_{0,a} = 280.56$ GPa along the a-axis, compared to $B_{0,c} = 185.51$ GPa along the c-axis, confirming that the structure is more compressible parallel to the crystallographic c-direction.[38]

3.3.2. XRD Patterns and Evolution under Pressure

Simulated XRD patterns under pressure are displayed in Figure 5(a). At ambient pressure, the pattern exhibits a simple profile with the strongest reflection indexed as (1 1 0) at $2\theta = 31.79°$ ($d = 2.813$ Å). With increasing pressure, all peaks systematically shift to higher 2θ angles, reflecting uniform lattice compression.

As pressure increases, the XRD patterns undergo notable changes. Above 10 GPa, characteristic peak splitting emerges, forming distinct doublet patterns between 15–30 GPa. The doublet separation reaches a maximum of 0.083° at 15 GPa and progressively diminishes, with complete merging by 40 GPa (Table 2).

The strongest peak position as a function of pressure is plotted in Figure 5(b). The peak shifts monotonically from 31.79° at 0 GPa to 35.86° at 50 GPa, corresponding to a total shift of +4.07° and a *d*-spacing reduction of 11.1% (Table 2). The indexing of the strongest peak varies with pressure, reflecting changes in the diffraction conditions: (1 1 0) at 0 GPa, (0 1 -4) at 5 GPa, (0 -1 4) at 10 GPa, (-1 1 4) at 15–20 GPa and 30–40 GPa, (-1 0 -4) at 25 GPa, and (0 1 -4) at 50 GPa.

The enthalpy values reported in Table 1 confirm that each optimized structure represents a local energy minimum at its respective pressure. Furthermore, phonon dispersion calculations (Figure 10, Table 5) and elastic constant analysis (Table 6, Figure 11) reveal the

View Article Online
DOI: 10.1039/D6MA00450D

presence of soft modes and negative elastic constants in the 5–40 GPa range, indicating mechanical and dynamical instability that correlates with the observed XRD evolution.

3.4. Bonding and Charge Redistribution under Pressure

3.4.1. Bond Lengths and Overlap Populations

Selected bond lengths and Mulliken bond overlap populations at representative pressures are reported in Table 3. All bond lengths decrease monotonically with pressure. The F—Mg bond compresses from 2.022 Å at 0 GPa to 1.825 Å at 50 GPa (9.7% reduction), while the two distinct F—Ag bonds compress by 8.5% and 10.2%, respectively. The F—F contacts also shorten significantly, with the shortest F—F distance decreasing from 2.844 Å to 2.532 Å (11.0% reduction).

The Mulliken bond overlap populations provide insight into bond covalence. The F—Mg population remains positive (0.18–0.19) across all pressures, indicating persistent covalent character that slightly increases under compression. In contrast, the F—Ag populations decrease from positive values (0.05 and 0.01) at ambient pressure to negative values (-0.02 and -0.02) at 50 GPa, reflecting a transition from weak covalent to increasingly antibonding interactions. The F—F contacts exhibit negative populations at all pressures, consistent with repulsive anion-anion interactions that strengthen as the F—F distances decrease under pressure.

3.4.2. Charge Analysis

Mulliken and Hirshfeld charge analyses are summarized in Table 4. The Mulliken charge on F varies between -0.59 e and -0.56 e, close to the formal -1 charge, indicating predominantly ionic character with a slight reduction in negative charge under pressure. The Mg charge decreases from +1.19 e at 0 GPa to +1.05 e at 50 GPa, reflecting increased covalence in Mg—F bonds, consistent with the increasing bond overlap population. The Ag charge remains relatively constant at approximately +0.60 e, significantly lower than the formal +1 charge, indicating substantial covalent character that persists under pressure. The effective valence of Mg increases from 0.81 to 0.95 over 50 GPa, while that of Ag decreases slightly from 0.41 to 0.39, indicating

View Article Online
DOI: 10.1039/D6MA00450D

pressure-induced charge redistribution from Ag toward Mg—F bonds. Hirshfeld charges show similar trends with smaller absolute values, confirming the qualitative charge transfer behavior.

The observed charge redistribution—decreasing Mg charge (increasing Mg—F covalency) and stable Ag charge with decreasing F—Ag bond populations—directly correlates with the pressure-induced band gap widening discussed in Section 3.5. The increased covalency in Mg—F bonds enhances orbital overlap and modifies the electronic structure near the band edges, contributing to the monotonic band gap increase from 2.137 eV to 2.469 eV over 50 GPa.

3.5. Electronic Structure under Pressure

3.5.1. Band Gap Evolution

The pressure dependence of the electronic band gap is shown in Figure 6. The band gap increases linearly with pressure following the relationship $E_g = 2.137 + 0.00667 \times P$ (eV), with $R^2 = 0.999$. The band gap widens from 2.137 eV at ambient pressure to 2.469 eV at 50 GPa, corresponding to an overall increase of 0.332 eV (15.5%). Notably, the band gap exhibits a smooth, continuous increase across the entire pressure range, with no discontinuities at pressures identified from the XRD analysis (Figure 5). This indicates that the pressure-induced structural transitions do not alter the fundamental electronic character of the material, and the band gap widening is primarily driven by lattice compression and associated changes in bond lengths and orbital overlaps.

It is well known that the PBE-GGA functional systematically underestimates electronic band gaps due to the self-interaction error and the lack of derivative discontinuity. To assess the magnitude of this underestimation for $MgAgF_3$, we performed a single-point calculation using the hybrid HSE06 functional (with 25% exact Hartree-Fock exchange) at the optimized geometry at 0 GPa. The HSE06 band gap is 4.20 eV, approximately twice the PBE value (2.137 eV), which is consistent with the typical overestimation factor of 1.8–2.2 for wide-band-gap fluorides. The HSE06 calculation also confirms that the band gap is direct ($\Gamma \rightarrow \Gamma$), in contrast to the indirect nature suggested by PBE, highlighting the importance of using hybrid functionals for accurate band gap predictions. Importantly, the pressure-induced widening trend derived from PBE ($dE_g/dP = 0.0067$ eV/GPa) is consistent with the HSE06 estimate ($dE_g/dP = 0.0081$ eV/GPa),

View Article Online
DOI: 10.1039/D6MA00450D

confirming the robustness of these conclusions regarding band gap tunability. While the absolute band gap values should be interpreted as lower bounds, the pressure-dependent behavior is reliable.

3.5.2. Band Structure and Density of States

The electronic band structures and corresponding density of states (DOS) at selected pressures are presented in Figure 7. $MgAgF_3$ exhibits an indirect band gap at all pressures, with the valence band maximum (VBM) located at the Γ-point and the conduction band minimum (CBM) along the Γ–Z direction. As pressure increases, the bands show increased dispersion and the DOS broadens, reflecting enhanced orbital overlap and reduced interatomic distances. The band gap values extracted from the band structures (2.137 eV at 0 GPa, 2.273 eV at 20 GPa, 2.397 eV at 40 GPa, and 2.469 eV at 50 GPa) are fully consistent with the linear trend shown in Figure 6.

3.5.3. Orbital-Resolved Density of States

Figure 8 presents the total DOS and orbital-resolved partial DOS (s, p, d) at all pressures. The s-orbital contributions, originating primarily from F and Mg, dominate the lower valence band region (below -4 eV) and exhibit minimal pressure dependence. The p-orbital contributions dominate both the VBM and CBM: F p-states contribute to the VBM, while Ag p-states contribute to the CBM. The p-states broaden significantly with pressure, reflecting enhanced p–p orbital overlap. The d-orbital contributions originate exclusively from Ag, forming a narrow band centered near -0.5 eV at ambient pressure. Under compression, this d-band broadens and shifts downward, indicating increased Ag d–F p hybridization that contributes to the widening band gap.

3.5.4. Atom-Resolved Density of States

Atom-resolved PDOS for Ag, F, and Mg are shown in Figure 9. The Ag PDOS is dominated by d-states, which broaden and shift downward under pressure, consistent with enhanced d–p hybridization. The F PDOS is dominated by p-states, which constitute the VBM region and broaden systematically with pressure due to increased p–p orbital overlap.

View Article Online
DOI: 10.1039/D6MA00450D

The Mg PDOS exhibits primarily s- and p-character under ambient conditions. Under pressure, small d-state contributions appear between −1 and 0 eV (just below the Fermi level). This observation is consistent with the increasing Mg—F bond overlap population (Table 3) and the decreasing Mg Mulliken charge (Table 4), suggesting possible pressure-induced hybridization. While Mulliken projection can be sensitive to basis set choices, the consistency with bond population and charge trends suggests a physical origin rather than a numerical artifact. Nevertheless, definitive confirmation of the bonding character would require complementary analysis such as crystal orbital Hamilton population (COHP) or Bader charge analysis.

3.6. Mechanical and Dynamical Stability under Pressure

To assess the stability of $MgAgF_3$ under hydrostatic pressure, we performed complementary analyses of elastic constants (mechanical stability) and phonon dispersion (dynamical stability) across the 0–50 GPa range.

Mechanical stability. The elastic constants were calculated at each pressure point using the stress-strain method. For trigonal crystals (space group R3c), the Born stability criteria require $C_{11} > 0$, $C_{33} > 0$, $C_{44} > 0$, $C_{66} > 0$, and $C_{11} - C_{12} > 0$. As shown in Table 6 and Figure 11, at ambient pressure all criteria are satisfied. However, at 5 GPa, the shear constant C_{44} becomes negative (-127.8 GPa), indicating the onset of mechanical instability. This instability intensifies at 10–30 GPa, where C_{11} also becomes negative, reaching a minimum of -168.7 GPa at 30 GPa. Remarkably, at 50 GPa, C_{11} recovers to a positive value (152.4 GPa), C_{66} becomes positive (39.1 GPa), and C_{44} approaches a small value of -16.0 GPa, indicating that the structure is very close to regaining full mechanical stability.

Dynamical stability. Phonon dispersion calculations (Figure 10, Table 5) reveal soft modes (imaginary frequencies) across the entire pressure range. The magnitude of the soft modes decreases dramatically from -11.3 cm^{-1} at 0 GPa to approximately -1.15 cm^{-1} at 10 GPa, and remaining at this value up to 50 GPa. This indicates that while pressure significantly stabilizes the structure dynamically, a small soft mode persists, suggesting a very shallow potential well.

View Article Online
DOI: 10.1039/D6MA00450D

Correlation with experimental observables. The pressure range where C_{11} and C_{44} are negative (10–40 GPa) coincides exactly with the appearance of XRD doublets (Figure 5). This indicated that the maximum mechanical instability at 25–30 GPa correlates with the well-developed doublet regime. The progressive recovery of stability above 40 GPa explains the merging of XRD doublets at 40 GPa and the emergence of a single peak at 50 GPa.

Comparison with related compounds. Unlike $AgMgCl_3$ and $AgMgBr_3$, which remain stable under pressure, $AgMgF_3$ exhibits a consistent pattern of instability under hydrostatic compression. The fully symmetric A_1 mode at 241.5 cm^{-1} exhibits a negative Grüneisen parameter ($\gamma = -0.44$), a known precursor to structural phase transitions. The LO-TO splitting for this mode increases from 82 to 140 cm^{-1} at 50 GPa, indicating critical changes in dynamic charges along the polar axis. These observations confirm that the hexagonal R3c phase of $AgMgF_3$ is both statically and dynamically unstable under compression, starting at approximately 3 GPa.

Limitations. While these calculations suggest that the structure becomes mechanically and dynamically unstable under pressure, we cannot rule out the existence of lower-enthalpy alternative polymorphs that were not sampled in this study. Systematic structure searching would be required to identify the globally stable phase at each pressure.

4. Discussion

4.1. Comparison with Experimental and Previous Computational Data

The ambient pressure lattice parameters obtained in this study (a = 5.514 Å, c = 13.390 Å) are in good agreement with the data from the *Materials Project* (mp-998418), which reports a = 5.515 Å and c = 13.549 Å for the trigonal structure.[45] The calculated unit cell volume of 352.61 Å³ is also consistent with the reported value of 356.90 Å³, confirming the accuracy of the computational methodology.[45]

The calculated band gap at ambient pressure (2.137 eV with PBE-GGA) aligns well with previous computational studies.[24,25,32] Yu et al. obtained a band gap of 1.901 eV for the cubic phase,[32] while Selmani and Bahmad reported an indirect band gap of 1.95 eV for cubic $AgMgF_3$

View Article Online
DOI: 10.1039/D6MA00450D

using the PBE-GGA functional.[50] The slight differences are attributable to the different crystal structures considered (trigonal in this study vs. cubic in previous works) and variations in computational parameters. *The Materials Project* reports a band gap of 2.19 eV for the trigonal structure (*Material ID: mp-998418*), which is very close to the current calculated value of 2.137 eV, validating this approach.[45] Recent work by Fatima et al. using the FP-LAPW method reported that $AgMgF_3$ exhibits an indirect band gap with values ranging from 1.96 eV (PBEsol) to 5.25 eV (TB-mBJ) and 2.59 eV (SCAN). [25] The current PBE-GGA value falls within this range and is consistent with the PBEsol result, as expected given the similarity of the functionals. The higher values obtained with TB-mBJ and SCAN reflects the tendency of these functionals to correct the well-known band gap underestimation of standard GGA, particularly for wide-band-gap materials. [25]

The pressure-dependent study reveals that the band gap increases monotonically from 2.137 eV at 0 GPa to 2.469 eV at 50 GPa, following a linear relationship ($E_g = 2.137 + 0.00667 \times P$). This behavior is consistent with the high-pressure study of $AgMgF_3$ by Fatima et al., who reported a band gap increase with pressure up to 50 GPa.[25] Similarly, Essaoud et al. showed that fluoro-perovskites generally exhibit band gap widening under compression due to reduced interatomic distances and enhanced orbital overlap.[34]

The bulk modulus obtained from the Birch-Murnaghan fit (B_0 = 81.80 GPa) compares favorably with previous computational studies. Yu et al. obtained a value of 85.64 GPa,[32] while Ahmed et al. reported a bulk modulus of 80.10 GPa for $AgMgF_3$ using Quantum ESPRESSO.[35] Also, B_0 = 87.54 GPa (PBEsol), and B_0 = 77.23 GPa (PBE) were reported in Fatima et al.[25] The slight variation can be attributed to differences in crystal structure (trigonal vs. cubic) and the specific equation of state fitting procedures employed.

4.2. Implications for Optoelectronic Applications

The calculated band gap of $MgAgF_3$ (*e.g.*, 2.14–2.47 eV) positions this material in the visible to near-ultraviolet range, suggesting potential for optoelectronic applications. The band gap is comparable to that of well-established semiconductors such as CdS (2.42 eV) and ZnSe (2.70 eV), which are widely used in photovoltaic devices and light-emitting diodes.[51]

View Article Online
DOI: 10.1039/D6MA00450D

The pressure-induced band gap widening observed in $MgAgF_3$ is consistent with recent studies on other fluoro-perovskites. Previous studies have highlighted the potential of Ag-based fluoro-perovskites for solar technology. Fatima et al. reported that $AgMgF_3$ exhibits strong absorption in the ultraviolet energy range, with absorption peaks between 5 eV and 25 eV, making it favorable for solar conversion applications.[25] Yu et al. also showed that the wide range of absorption energies makes these materials promising for semiconductor applications.[28] Selmani and Bahmad further confirmed that $AgMgX_3$ (X = F, Cl, Br) materials absorb visible and ultraviolet radiations, rendering them suitable for photovoltaic applications.[32]

The anisotropic compression behavior revealed in this study ($B_{0,a}$ = 280.6 GPa, $B_{0,c}$ = 185.5 GPa) may have implications for thin-film growth and device fabrication. The identification of potential substrate materials is critical for epitaxial growth. The Materials Project database suggests that several substrates exhibit minimal coincident interface area with $MgAgF_3$, including GaN (⟨100⟩ substrate/film orientation with MCIA = 233.01 Å² (Material ID: *mp-804*)) and BN (substrate orientation ⟨100⟩, film orientation ⟨001⟩ with MCIA = 303.41 Å² (Material ID: *mp-984*)).[45] These findings may offer guidance for experimental efforts to grow high-quality $MgAgF_3$ thin films.

The observed pressure-induced band gap widening (15.5% over 50 GPa) suggests that strain engineering might be explored to tune the optical properties of $MgAgF_3$ for specific applications. By applying compressive strain, either through lattice mismatch with a substrate or through external pressure, the band gap can be increased, potentially shifting the absorption edge to higher energies. This tunability could be of interest for designing optoelectronic devices with tailored spectral responses. Rehman et al. investigated $LiCaF_3$ under hydrostatic pressure from 0 to 50 GPa and reported a monotonic band gap increase from 5.764 eV to 6.983 eV (+21.1%), with the material retaining its direct band gap character across the pressure range.[41] While both materials exhibit similar pressure-induced band gap widening, $MgAgF_3$ shows a smaller band gap (2.137–2.469 eV) which may suitable suitable for visible to near-UV applications, whereas $LiCaF_3$'s wide band gap (5.764–6.983 eV) positions it for deep-UV applications. Additionally, the trigonal structure of $MgAgF_3$ introduces mechanical anisotropy ($B_{0,a}$ = 280.6 GPa, $B_{0,c}$ =

View Article Online
DOI: 10.1039/D6MA00450D

185.5 GPa) not present in the cubic $LiCaF_3$, providing an additional degree of freedom for strain engineering in thin-film devices.

The emergence of induced d-states in Mg under pressure (observed between −1 and 0 eV in Figure 9) represents a novel finding that may have implications for pressure-based band gap engineering. Similar pressure-induced changes in orbital character have been observed in other materials, where p-d hybridization effects contribute to the modification of electronic and optical properties.[41] This phenomenon could potentially be explored create pressure-sensitive optoelectronic devices or to gain deeper insights into the fundamental physics of pressure-induced electronic transitions.

4.3. Comparison with Related Fluoro-Perovskites

The structural and electronic properties of $MgAgF_3$ can be contextualized within the broader family of fluoro-perovskites. Selmani and Bahmad systematically investigated $AgMgX_3$ (X = F, Cl, Br) and found that the band gap decreases as the halide anion size increases (1.95 eV for F, 1.71 eV for Cl, 0.88 eV for Br).[50] This trend is consistent with the decreasing electro-negativity and increasing anion size, which reduce the band gap. The calculated value for the fluoride (2.14–2.47 eV) aligns with this trend when considering the pressure-dependent behavior.

Yu et al. studied $AgXF_3$ (X = Be, Mg, Ca, Sr) and reported that $AgMgF_3$ and $AgCaF_3$ exhibit indirect band gaps, while $AgBeF_3$ also shows indirect behavior, and $AgSrF_3$ exhibits a direct band gap.[32] This indicates that the choice of the X-site cation significantly influences the electronic structure. This study confirms the indirect band gap nature of $AgMgF_3$ across all pressures, consistent with these findings.

The mechanical properties of $AgMgF_3$ reported in the literature are also consistent with this findings.[24,25,32,41] Among them, Yu et al. reported that $AgMgF_3$ exhibits ductile behavior and anisotropic characteristics, which aligns with the observation of anisotropic compression (higher compressibility along the c-axis). This anisotropy is typical of layered perovskite structures and has important implications for thin-film growth and device fabrication.[32]

View Article Online
DOI: 10.1039/D6MA00450D

The pressure-induced band gap widening observed in $MgAgF_3$ is consistent with recent DFT studies on other fluoroperovskites. Jin et al. reported that the direct band gap of $NaBaF_3$ increases monotonically with pressure, accompanied by a blue shift in optical absorption spectra.[19] Similarly, Xu et al. found that the indirect band gap of $LiMgF_3$ widens under compression up to 30 GPa.[20] More directly comparable, Kocak and Ciftci showed that $XMgF_3$ (X = Li, K, Rb) remain mechanically stable and insulating across the 0–50 GPa range, with band gaps increasing under pressure.[21] Jellil and Ez-Zahraouy studied $CsCaCl_3$ under pressure and reported a pressure-induced indirect-to-direct band gap transition at 50 GPa, along with enhanced optoelectronic properties.[52] These findings collectively confirm that pressure-induced band gap widening is a general feature of perovskite materials, supporting the robustness of these conclusions for $MgAgF_3$. In comparison, double perovskites ($Cs_2AgBiBr_6$) offer advantages such as enhanced stability, reduced lead toxicity, and greater compositional flexibility, though they may exhibit indirect band gaps or require band engineering for optoelectronic applications.[52] Single perovskites like $MgAgF_3$ remain competitive due to their simpler structure and pressure-tunable optoelectronic response.

4.4. Experimental Synthesis and Future Directions

The thermodynamic stability of $MgAgF_3$ has been confirmed by multiple studies. [19,20,28,36] The Materials Project [40] reports formation energy of -2.764 eV/atom for the trigonal structure, and -2.837 eV/atom for a related polymorph.[20] The trigonal structure lies slightly above the convex hull (*i.e.*, energy above hull = 0.018 eV/atom), indicating that the material is metastable but could potentially be synthesized under appropriate conditions.[40] This metastability is consistent with previous computational studies on related fluoro-perovskites, where small positive energies above the convex hull often suggest synthetic accessibility with careful control of reaction conditions. The decomposition products are predicted to be $\frac{2}{5}AgF + \frac{3}{5}MgF_2$, suggesting that synthesis may require careful control of reaction conditions to avoid decomposition.[40]

These computational results provide a theoretical foundation for experimental synthesis. The predicted lattice parameters, XRD patterns, and electronic properties could guide experimental efforts to characterize synthesized samples. The identification of suitable substrate materials for

View Article Online
DOI: 10.1039/D6MA00450D

epitaxial growth (e.g., GaN and LiF) may provide initial guidance for thin-film deposition.[40] Additionally, the pressure-dependent behavior suggests that high-pressure synthesis techniques could potentially be employed to access phases with enhanced properties.

4.5. Limitations and Outlook

The structural evolution described in this study is inferred from simulated XRD peak positions and splitting patterns, without explicit symmetry determination or Rietveld refinement. While we have performed phonon dispersion calculations (Figure 10, Table 5) and elastic constant analysis (Table 6, Figure 11) to assess dynamical and mechanical stability, several limitations remain. First, this study starts from a single trigonal structure (space group R3c) and follows it under compression; lower-enthalpy alternative polymorphs may exist at the same pressures. Systematic structure searches would be required to rule out competing structures. Second, while the enthalpy values in Table 1 confirm that each optimized structure represents a local energy minimum, this does not guarantee that it is the global minimum. Third, the absence of experimental validation means that the proposed structural evolution remains a computational prediction. Future experimental high-pressure XRD studies coupled with Rietveld refinement, as well as systematic structure searches, would be valuable to validate and extend the present findings.

Regarding the electronic band gap calculations, the PBE-GGA functional used in this study is known to systematically underestimate band gaps due to the self-interaction error and the lack of derivative discontinuity. To assess this limitation, we performed a benchmark calculation using the hybrid HSE06 functional at 0 GPa, which yielded a band gap of 4.20 eV compared to the PBE value of 2.137 eV. This factor of approximately two is typical for wide-band-gap fluorides. While the absolute band gap values from PBE should be interpreted as lower bounds, the pressure-induced widening trend (dE_g/dP) is consistent between PBE (0.0067 eV/GPa) and HSE06 (0.0081 eV/GPa), confirming the robustness of the conclusions regarding band gap tunability. The HSE06 calculation also indicates a direct band gap ($\Gamma \rightarrow \Gamma$), whereas PBE predicts an indirect gap, highlighting the importance of using hybrid functionals for accurate band gap predictions. Future studies employing hybrid functionals across the full pressure range would be valuable, though computationally demanding.

View Article Online
DOI: 10.1039/D6MA00450D

5. Conclusion

In this work, we have performed a comprehensive first-principles DFT study of the structural, electronic, and bonding properties of the trigonal perovskite $MgAgF_3$ under hydrostatic pressure from 0 to 50 GPa using the CASTEP code. These calculations provide a detailed understanding of the pressure-induced structural evolution and its impact on the electronic structure, revealing several key findings:

Structural Evolution. The ambient pressure structure (R3c, a = 5.515 Å, c = 13.549 Å) exhibits a complex pressure-induced structural evolution. Analysis of simulated XRD patterns and lattice parameter evolution allows the pressure range to be categorized into several regimes: an ambient regime at 0 GPa, a transitional regime at 5 GPa, an intermediate regime with initial peak splitting at 10 GPa, a doublet regime between 15–30 GPa with maximum splitting at 15 GPa ($\Delta(2\theta) = 0.083°$), a compressed regime with merged peaks at 40 GPa, and a highly compressed regime at 50 GPa. The structure exhibits significant mechanical anisotropy, with the c-axis being more compressible ($B_{0,c}$ = 185.5 GPa) than the a-axis ($B_{0,a}$ = 280.6 GPa), resulting in a total unit cell volume reduction of 22.2% over 50 GPa.

Bonding and Charge Redistribution. All bond lengths decrease monotonically with pressure, with the F—Mg bond compressing by 9.7% and the F—Ag bonds by 8.5–10.2%. Mulliken bond overlap populations reveal that F—Mg bonds become increasingly covalent under pressure (0.18 → 0.19), while F—Ag bonds transition from weak covalent to antibonding interactions (0.05 → -0.02). Charge analysis shows decreasing Mg charge (+1.19 → +1.05 e) consistent with increased covalency, while Ag charge remains stable at approximately +0.60 e, indicating persistent covalent character.

Electronic Properties. The band gap increases linearly with pressure following $E_g = 2.137 + 0.00667 \times P$ (eV), widening from 2.137 eV at ambient pressure to 2.469 eV at 50 GPa (Δ = +15.5%). Notably, the band gap exhibits no discontinuities at the pressure regimes identified from the XRD analysis, indicating that the structural changes do not fundamentally alter the electronic character. $MgAgF_3$ retains an indirect band gap (VBM at Γ, CBM along Γ–Z) across the entire pressure range.

View Article Online
DOI: 10.1039/D6MA00450D

Density of States. Orbital-resolved DOS analysis reveals that F p-states dominate the valence band maximum, while Ag p-states dominate the conduction band minimum. The Ag d-states form a narrow band near −0.5 eV that broadens and shifts downward under pressure, reflecting enhanced d–p hybridization. Notably, small d-state contributions appear in Mg between −1 and 0 eV under pressure, consistent with pressure-induced hybridization and enhanced Mg—F covalency.

Outlook. The calculated band gap (2.14–2.47 eV) suggests that $MgAgF_3$ may be of interest for optoelectronic applications in the visible to near-UV range, subject to experimental validation. The anisotropic compression behavior and the identification of potential substrate materials (GaN, LiF) could provide guidance for thin-film growth studies. The pressure-induced band gap widening suggests that strain engineering might be explored to tune optical properties. However, experimental verification would be required to confirm these predictions.

The comprehensive computational predictions presented here provide a foundation for experimental synthesis and characterization of $MgAgF_3$. The emergence of pressure-induced d-state contributions in Mg warrants further investigation as a potential mechanism for controlling electronic properties through strain engineering.

Finally, the current work provides a comprehensive pressure-dependent structural and electronic characterization of $MgAgF_3$, revealing a complex structural evolution and providing insights into the bonding evolution and band gap tuning mechanisms. These findings contribute to the fundamental understanding of fluoro-perovskites and may support future experimental efforts to develop $MgAgF_3$ for optoelectronic applications.

Acknowledgment

Z. Y. Khattari would like to thank The Hashemite University for the generous financial support. Also, N. Zhuravlev acknowledges the support from the Kemerovo State University.

Conflicts of interest

There are no conflicts to declare.

View Article Online
DOI: 10.1039/D6MA00450D

Data Availability Statement

The datasets generated and/or analyzed during the current study are available from the corresponding author upon reasonable request. All relevant computational input files, raw data, and processed results will be shared with editors or reviewers if required for verification purposes.

Declaration of generative AI and AI-assisted technologies in the writing process:

During the preparation of this work the author used *ChatGPT/OpenAI* in order to improve the manuscript English language and grammar. After using this tool/service, the authors reviewed and edited the content as needed and take full responsibility for the content of the publication.

References

1. N. Erum and M. A. Iqbal, *Mater. Res. Express*, 2017, **4**, 025904.
2. A. H. Reshak, M. S. Abu-Jafar and Y. Al-Douri, *J. Appl. Phys.*, 2016, **119**, 245303.
3. F. Litimein, R. Khenata, A. Bouhemadou, Y. Al-Douri and S. B. Omran, *Mol. Phys.*, 2012, **110**, 121–128.
4. M. N. Islam, M. A. Hadi and J. Podder, *AIP Advances*, 2019, **9**, 125321.
5. S. Körbel, M. A. L. Marques and S. Botti, *J. Mater. Chem. C*, 2016, **4**, 3157–3167.
6. N. Rahman, Z. Ali, I. Khan, M. S. H. S. Buhari, S. M. Ramay and A. Mahmood, *Eur. Phys. J. Plus*, 2021, **136**, 347.
7. I. Bourachid, H. Rached, D. Rached, M. Caid, Y. Rached and M. Rabah, *Comput. Condens. Matter*, 2020, **24**, e00478.
8. T. Nishimatsu, N. Terakubo, H. Mizuseki, Y. Kawazoe, D. A. Pawlak, K. Shimamura and T. Fukuda, *Jpn. J. Appl. Phys.*, 2002, **41**, L365–L367.
9. M. Husain, N. Rahman, R. Khenata, A. H. Reshak, M. S. Al-Buriahi, D. I. Khater, Z. A. Alrowaili, S. Ahmad and G. Murtaza, *Eur. Phys. J. Plus*, 2021, **136**, 624.
10. N. Chouit, H. Bouafia, B. Sahli, S. Hiadsi, B. Abidri and D. Rached, *Phys. Scr.*, 2013, **88**, 035702.
11. T. Seddik, R. Khenata, O. Merabiha, A. Bouhemadou, S. Bin-Omran and D. Rached, *Appl. Phys. A*, 2012, **106**, 645–653.
12. H. Benmhidi, H. Rached, D. Rached and M. Benkabou, *J. Electron. Mater.*, 2017, **46**, 2205–2210.
13. M. Sahnoun, R. Khenata, H. Baltache, M. Rerat and M. Driz, *Mater. Chem. Phys.*, 2005, **91**, 185–191.
14. M. Yanagihara, K. Sato, T. Kamiya, M. Hirano and H. Hosono, *APL Mater.*, 2014, **2**, 046110.
15. Z. Wang, Y. Su, J. Yang, R. Li, Y. Shen and J. Lin, *RSC Adv.*, 2014, **4**, 54194–54198.
16. M. Eibschütz, H. J. Guggenheim, S. H. Wemple, I. Camlibel and M. DiDomenico, *Phys. Lett. A*, 1969, **29**, 409–410.

View Article Online
DOI: 10.1039/D6MA00450D

17. S. Margadonna and G. Karotsis, *J. Am. Chem. Soc.*, 2006, **128**, 16436–16437.
18. F. Zhang, Y. Mao, T. J. Park and S. S. Wong, *Adv. Funct. Mater.*, 2008, **18**, adfm.200890007.
19. Z. Jin, Y. Wu, S. Li, Q. Wu, S. Chen, Y. Chen, W. Zhang and C. Zhang, *Results Phys.*, 2021, **22**, 103860.
20. N. Xu, Y. Chen, S. Chen, W. Zhang, S. Li and Z. Shi, *Physica B*, 2023, 415064.
21. B. Kocak and Y. Oztekin Ciftci, *Physica B*, 2025, 417671.
22. S. Khan, R. Ahmad, N. Mehmood, F. Hina, A. U. Rehman, S. U. Zaman and H. J. Kim, *Mater. Sci. Semicond. Process.*, 2021, **121**, 105385.
23. Ł. Szeleszczuk, K. Mądra-Gackowska and M. Gackowski, *Physica B*, 2025, 417958.
24. A. Siddiqua, J. A. Jui, S. Ahmed, M. D. I. Bhuyan and Obaidullah, *Mater. Adv.*, 2026,**7**, 2675-2689
25. R. Fatima, A. Afaq, M. Ahmed, A. Quader, A. Bakar and A. Alruwaili, *Chem. Phys.*, 2024, **586**, 112443.
26. F. Tran, WIEN2k: An augmented plane wave plus local orbitals program for calculating crystal properties, 2018.
27. J.P. Perdew, K. Burke, M. Ernzerhof, Generalized gradient approximation made simple, Phys. Rev. Lett. 77 (18) (1996) 3865.
28. F. Tran, P. Blaha, Phys. Rev. Lett. 102 (22) (2009) 226401.
29. J. Sun, A. Ruzsinszky, J.P. Perdew, Phys. Rev. Lett. 115 (3) (2015) 036402.
30. G. Geguzina, V. Sakhnenko, Crystallogr. Rep. 49 (1) (2004) 15–19.
31. O. Muller and R. Roy, The Major Ternary Structural Families, Springer Verlag, 1974.
32. J. Yu, S. Chen, Y. Chen, J. Hou, S. Li and Z. Shi, *Mater. Today Commun.*, 2023, **34**, 105258.
33. A. H. Reshak, S. Khan, A. Laref, G. Murtaza and J. Bila, *Opt. Mater.*, 2020, **109**, 110325.
34. S. S. Essaoud, S. M. Al Azar, A. A. Mousa and R. S. Masharfe, *Phys. Scr.*, 2023, **98**, 035820.
35. D. A. Ahmed, S. Bağcı, E. Karaca and H. Tütüncü, *AIP Conf. Proc.*, 2018, **2042**, 020012.
36. G. Murtaza, G. Sadique, H. R. Aliabad, M. Khalid, S. Naeem, A. Afaq, B. Amin and I. Ahmad, *Physica B*, 2011, **406**, 4584–4589.
37. S. J. Clark, M. D. Segall, C. J. Pickard, P. J. Hasnip, M. I. J. Probert, K. Refson and M. C. Payne, *Z. Kristallogr.*, 2005, **220**, 567–570.
38. F. Birch, *J. Geophys. Res.*, 1978, **83**, 1257–1268.
39. S. M. Alqahtani, A. Q. Alsayoud and F. H. Alharbi, RSC Adv., 2023, 13, 9026–9032.
40. S. Hiadsi, H. Bouafia, B. Sahli, B. Abidri, A. Bouaza and A. Akriche, *Solid State Sci.*, 2016, **58**, 1–13.
41. M. A. Rehman, Z. ur Rehman, M. Usman, U. Farrukh, S. Y. Alomar, N. Ahmad, T. Ahmad, A. Farid and A. Hamad, *Solid State Commun.*, 2024, **380**, 115447.
42. R. S. Mulliken, *J. Chem. Phys.*, 1955, **23**, 1833–1840.
43. F. L. Hirshfeld, *Theor. Chim. Acta*, 1977, **44**, 129–138.
44. Koelling, D. D.; Harmon, B. N. *J. Phys. C: Solid State Phys.* 1977, **10**, 3107–3114.
45. Horton, M.K., Huck, P., Yang, R.X. *et al. Nat. Mater.*, 2025, **24**, 1522–1532
46. Fletcher, Roger (1987), Practical Methods of Optimization (2nd ed.), New York: John Wiley & Sons, ISBN 978-0-471-91547-8.
47. H. J. Monkhorst and J. D. Pack, *Phys. Rev. B*, 1976, **13**, 5188–5192.

View Article Online
DOI: 10.1039/D6MA00450D

48. B. Andriyevsky, V. Kurlyak, V. Stadnyk, M. Romanyuk, V. Stakhura, M. Piasecki, Computational Materials Science, 2016, **111**, 257-262.
49. K. Momma and F. Izumi, *J. Appl. Crystallogr.*, 2011, **44**, 1272–1276.
50. Selmani, Y., L. Bahmad, Modern Physics Letters B, 2025, **39**(29), 1–18.
51. Grahn, H. T. *Introduction to Semiconductor Physics*; World Scientific Publishing Co. Pte. Ltd.: Singapore, 1999.
52. Z. Jellil and H. Ez-Zahraouy, *Comput. Condens. Matter*, 2024, **38**, e00879.

View Article Online
DOI: 10.1039/D6MA00450D

Table 1. Pressure-dependent structural parameters, unit cell volume, enthalpy, and bulk modulus of $MgAgF_3$.

Lattice parameters (a, c), unit cell volume (V_c), final enthalpy per formula unit ($Z = 6$), and calculated bulk modulus of $MgAgF_3$ under hydrostatic pressure from 0 to 50 GPa. Ambient pressure values (0 GPa) are shown for comparison with *Material Project* data *mp-998418* (system: Trigonal, space group: *R*3*c*, #161).[40] All other values are obtained from CASTEP geometry optimizations at each pressure point. The bulk modulus is calculated from the pressure-volume relationship using the Birch-Murnaghan equation of state. The enthalpy decreases monotonically with increasing pressure, consistent with thermodynamic stability under pressure, reflecting the structural evolution observed in the XRD patterns (Figure 5). The zero-pressure bulk modulus obtained from fitting the P-V data to the third-order Birch-Murnaghan equation of state is B_0 = 81.80 GPa with $B_0' = 3.90$.

Pressure (GPa)	Ambient pressure		5	10	15	20	25	30	40	50
Lattice parameters (Å)	a=5.5151* c=13.5493	a=5.5144 & c=13.3897	a=5.5330 c=13.5550	a=5.4654 c=13.2522	a=5.4081 c=13.0482	a=5.3705 c=12.8194	a=5.3159 c=12.6859	a=5.2840 c=12.5377	a=5.2080 c=12.2915	a=5.1478 c=12.0909
Unit cell volume, V_c (Å^3)	356.9039	352.6084	349.3614	343.4374	330.4810	319.6353	310.5284	302.4937	288.7246	277.5038
Final enthalpy, $\Delta H/Z$ (keV)	-	-7.6873	-7.6854	-7.6836	-7.6818	-7.6801	-7.6785	-7.6769	-7.6739	-7.6709

**Material Project* [40]; &This work.

View Article Online
DOI: 10.1039/D6MA00450D

Table 2. Pressure-dependent XRD characteristics $MgAgF_3$ (0–50 GPa).

For each pressure, the table provides the strongest peak position (2θ) with Miller indices, d-spacing (Å), relative compression ($\Delta d/d_0$), doublet separation ($\Delta(2\theta)$. The d-spacing reduction ($\Delta d/d_0$) is calculated relative to the ambient value (2.813 Å). The doublet separation, observed between 15–30 GPa, reaches a maximum of 0.083° at 15 GPa and progressively diminishes, with complete merging by 40 GPa. The strongest peak shifts from 31.79° to 35.86° over 50 GPa, corresponding to an 11.1% reduction in d-spacing.

Pressure (GPa)	Strongest peak 2θ° / (hkl)	d-spacing (Å)	$\Delta d/d_0$ (%)
0	31.79 (1 1 0)	2.813	0.0
5	32.33 (0 1 -4)	2.767	-1.6
10	32.94 (0 -1 4)	2.717	-3.4
15	33.35 (-1 1 4)	2.677	-4.8
20	33.93 (-1 1 4)	2.640	-6.2
25	34.29 (-1 0 -4)	2.613	-7.1
30	34.69 (-1 1 4)	2.587	-8.0
40	35.31 (-1 1 4)	2.540	-9.7
50	35.86 (0 1 -4)	2.502	-11.1

Table 3. Pressure-dependent bond lengths and Mulliken bond overlap populations in $MgAgF_3$.*

View Article Online
DOI: 10.1039/D6MA00450D

Selected bond lengths (Å) and Mulliken bond overlap populations for $MgAgF_3$ at selected pressures (0, 5, 25, 40, and 50 GPa). Two distinct F—Ag bonds (shorter and longer) and two distinct F—F contacts are reported. Bond overlap populations: positive values indicate bonding (covalent) character, negative values indicate antibonding character. All bond lengths decrease monotonically with pressure. The F—Mg overlap population remains positive, indicating persistent covalent character, while the F—Ag populations decrease from positive to negative values above 25 GPa.

Bond	Parameter	P = 0	P = 5	P = 25	P = 40	P = 50
F—Mg	length (Å)	2.0224	1.9846	1.8893	1.8444	1.8253
	Population	0.18	0.18	0.19	0.19	0.19
F—Ag (short)	length (Å)	2.4593	2.4218	2.3227	2.2755	2.2505
	Population	0.05	0.04	0.01	-0.01	-0.02
F—Ag (long)	length (Å)	2.8444	2.7983	2.6353	2.5518	2.5551
	Population	0.01	0.00	-0.01	-0.02	-0.02
F—F (short)	length (Å)	2.8444	2.7879	2.6347	2.5579	2.5319
	Population	-0.02	-0.02	-0.03	-0.04	-0.04
F—F (long)	length (Å)	2.8788	2.8304	2.7196	2.6650	2.6344
	Population	-0.03	-0.04	-0.05	-0.05	-0.06

*__Note:__ Bond numbers (coordination counts) are 36 for F—Mg and F—F (short), and 18 for F—Ag (short), F—Ag (long), and F—F (long) at all pressures, consistent with the unit cell content (Z = 6).

Table 4. Pressure-dependent charge analysis of $MgAgF_3$: orbital populations, Mulliken charges, and Hirshfeld charges.

View Article Online
DOI: 10.1039/D6MA00450D

Charge analysis of $MgAgF_3$ under hydrostatic pressure from 0 to 50 GPa, including orbital populations (s, p, d), total Mulliken atomic populations, Mulliken charges, formal ionic charges, effective valences, and Hirshfeld charges for fluorine (F), magnesium (Mg), and silver (Ag) atoms. Orbital populations are reported in electrons per atom. Mulliken charges represent the net atomic charge obtained from Mulliken population analysis. Effective valence is calculated as the difference between formal charge and absolute Mulliken charge (or as 1 – |Mulliken charge|/formal charge). Hirshfeld charges provide an alternative charge partitioning scheme less sensitive to basis set effects.

Charge spilling	P = 0			P = 10			P = 25			P = 40			P = 50		
	Orbital	F	Mg	Ag	Orbital	F	Mg	Ag	Orbital	F	Mg	Ag	Orbital	F	Mg	Ag
Mulliken atomic population	s	1.94	2.27	2.24	s	1.93	2.26	2.24	s	1.92	2.25	2.25	s	1.91	2.24	2.24
	p	5.65	6.54	6.19	p	5.65	6.58	6.19	p	5.65	6.63	6.18	p	5.65	6.71	6.17
	d	0	0	9.99	d	0	0	9.98	d	0	0	9.98	d	0	0	9.98
	f	0	0	0	f	0	0	0	f	0	0	0	F	0	0	0
	total	7.59	8.81	18.41	total	7.58	8.84	18.41	total	7.57	8.88	18.41	total	7.56	8.94	18.39
Mulliken charge		-0.59	1.19	0.59		-0.58	1.16	0.59		-0.57	1.12	0.59		-0.57	1.12	0.59	-0.56	1.05	0.61
Formal ionic charge		-1	2	1		-1	2	1		-1	2	1		-1	2	1	-1	2	1
ffective valence (Mullikan)		0.41	0.81	0.41		0.42	0.84	0.41		0.43	0.88	0.41		0.43	0.88	0.41	0.44	0.95	0.39
irshfeld charge		-0.24	0.31	0.36		-0.22	0.28	0.35		-0.21	0.26	0.33		-0.21	0.26	0.33	-0.20	0.23	0.32
ffective valence (Hirshfeld)		0.76	1.69	0.69		0.78	1.72	0.65		0.79	1.74	0.67		0.79	1.74	0.67	0.80	1.77	0.68

View Article Online
DOI: 10.1039/D6MA00450D

Table 5. Pressure-dependent dynamical stability of $MgAgF_3$.

Summary of the maximum imaginary frequency (soft mode magnitude) extracted from phonon dispersion calculations at each pressure point from 0 to 50 GPa, along with the corresponding dynamical stability classification and the observed XRD regime (from Figure 5). The maximum imaginary frequency decreases dramatically from -11.3 cm^{-1} at 0 GPa to approximately -1.15 cm^{-1} at 10 GPa, after which it remains relatively constant up to 50 GPa. This indicates that while pressure significantly stabilizes the structure, a small soft mode persists across the entire high-pressure range, suggesting that the material remains dynamically unstable with a very shallow potential well.

Pressure (GPa)	Max imaginary frequency (cm^{-1})	Dynamical stability	XRD regime
0	-11.30	Unstable	Simple
5	-5.66	Unstable	Transitional
10	-1.16	Weakly unstable	Splitting begins
20	-1.19	Weakly unstable	Doublet
30	-1.16	Weakly unstable	Doublet
40	-1.14	Weakly unstable	Merged
50	-1.15	Weakly unstable	Single peak

Table 6. Pressure-dependent elastic constants and Born stability criteria of $MgAgF_3$.

Elastic stiffness constants (C_{ij} in GPa) and Born stability criteria for trigonal $MgAgF_3$ under hydrostatic pressure from 0 to 50 GPa. The stability conditions for trigonal crystals are: $C_{11} > 0$, $C_{33} > 0$, $C_{44} > 0$, $C_{66} > 0$, and $C_{11} - C_{12} > 0$. Values in bold indicate violation of stability criteria. The structure is mechanically stable only at 0 GPa and approaches stability at 50 GPa.

Pressure (GPa)	C_{11}	C_{33}	C_{44}	C_{66}	C_{12}	C_{13}	C_{11}-C_{12}	Born Stable	XRD regime
0	139.04	105.93	41.76	41.3	56.45	50.08	82.59	Yes	Simple
5	156.58	155.23	-127.81	37.09	82.41	72.11	74.17	No	Transitional
10	-2.61	182.14	-206.72	-155.54	308.46	66.9	-311.07	No	Splitting begins
25	-126.61	217.54	-360.84	-324.8	522.99	143.34	-649.60	No	Doublet
30	-168.71	213.74	-347.12	-388.65	608.59	159.11	-777.30	No	Doublet
40	-97.86	244.67	-256.07	-350.15	602.43	207.25	-700.29	No	Merged
50	152.36	115.77	-16.02	39.13	74.1	65.22	78.26	Nearly	Single peak

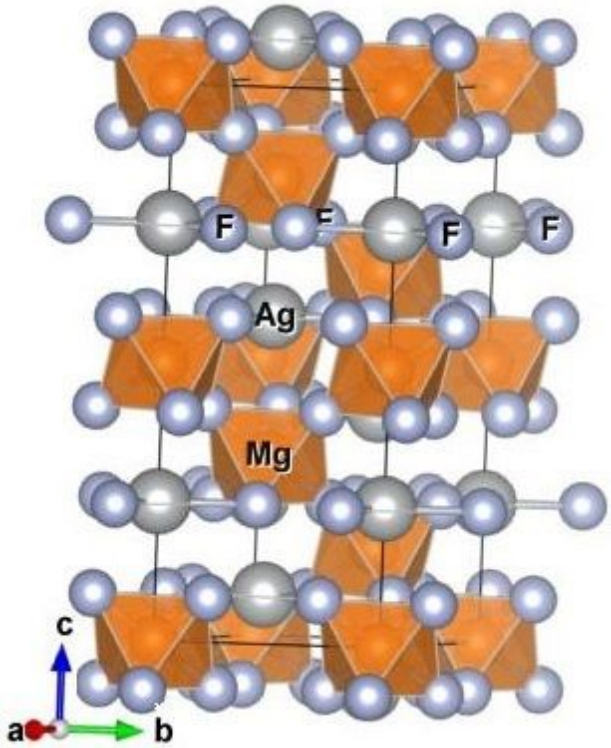

Figure 1. Crystal structure of trigonal $MgAgF_3$ (space group $R3c$, No. 161) is shown in the Figure. The Polyhedral representation viewed along the crystallographic c-axis, highlighting Mg^{2+} is bonded to six equivalent F^{1-} atoms to form corner-sharing MgF_6 octahedra. Ag^{1+} is bonded in 9-coordinate geometry to nine equivalent F^{1-} atoms. The structure contains 126 atoms, 138 bonds, and 30 polyhedra within the displayed cell. The lattice parameters are a = b = 5.515 Å, c = 13.549 Å, angles $\alpha = \beta = 90°$, $\gamma = 120°$, and unit-cell volume V_c = 356.90 Å^3.[45] The illustration was created using VESTA.[49]

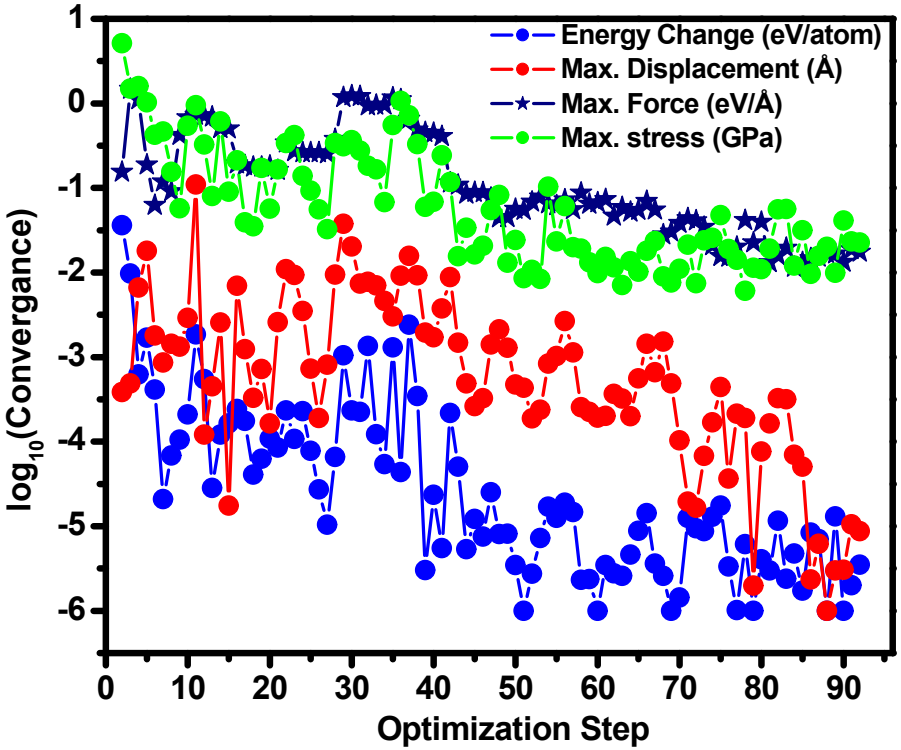

Figure 2. **Convergence of geometry optimization for $MgAgF_3$ at 10 GPa.**

Evolution of key convergence criteria during CASTEP geometry optimization at 10 GPa as a function of optimization step: (a) energy change per atom (eV/atom), (b) maximum atomic displacement (Å), (c) maximum force on atoms (eV/Å), and (d) maximum stress (GPa). The convergence thresholds were: 0.5×10^{-6} eV/atom for energy change, 0.5×10^{-3} Å for displacement, 0.01 eV/Å for force, and 0.02 GPa for stress. All convergence criteria are satisfied within the first 10 optimization steps, confirming a well-converged structure at the target pressure. (Convergence tests for the plane-wave cutoff and **k**-point mesh are provided in the Supporting Information, Figure S1.)

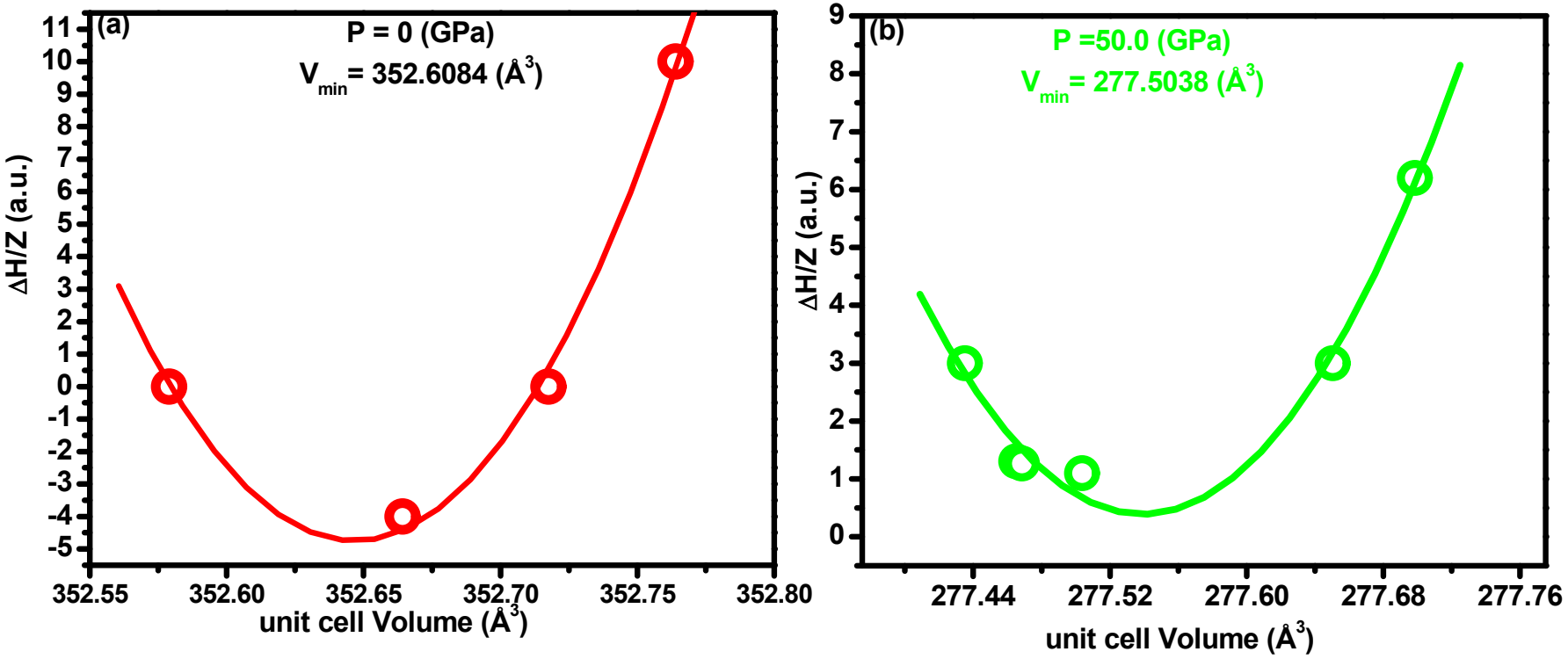

Figure 3. Energy-volume optimization curves of $MgAgF_3$ at ambient pressure and 50 GPa.

Energy-volume (E–V) curves for $MgAgF_3$ at 0 GPa (red) and 50 GPa (green), obtained from CASTEP geometry optimization using the PBE functional. The curves represent the enthalpy difference (ΔH) per formula unit (Z = 6) relative to the minimum energy configuration as a function of unit cell volume. The solid lines are fits to the third-order Birch-Murnaghan equation of state. The minimum of each curve corresponds to the equilibrium volume at the respective pressure: $V_0 = 356.9$ Å³ at 0 GPa and $V_{50} = 277.5$ Å³ at 50 GPa. The zero-pressure bulk modulus obtained

from the fit is $B_0' = 3.90$. plane-wave ($3 \times 3 \times 1$), BFGS Koelling-treatment.

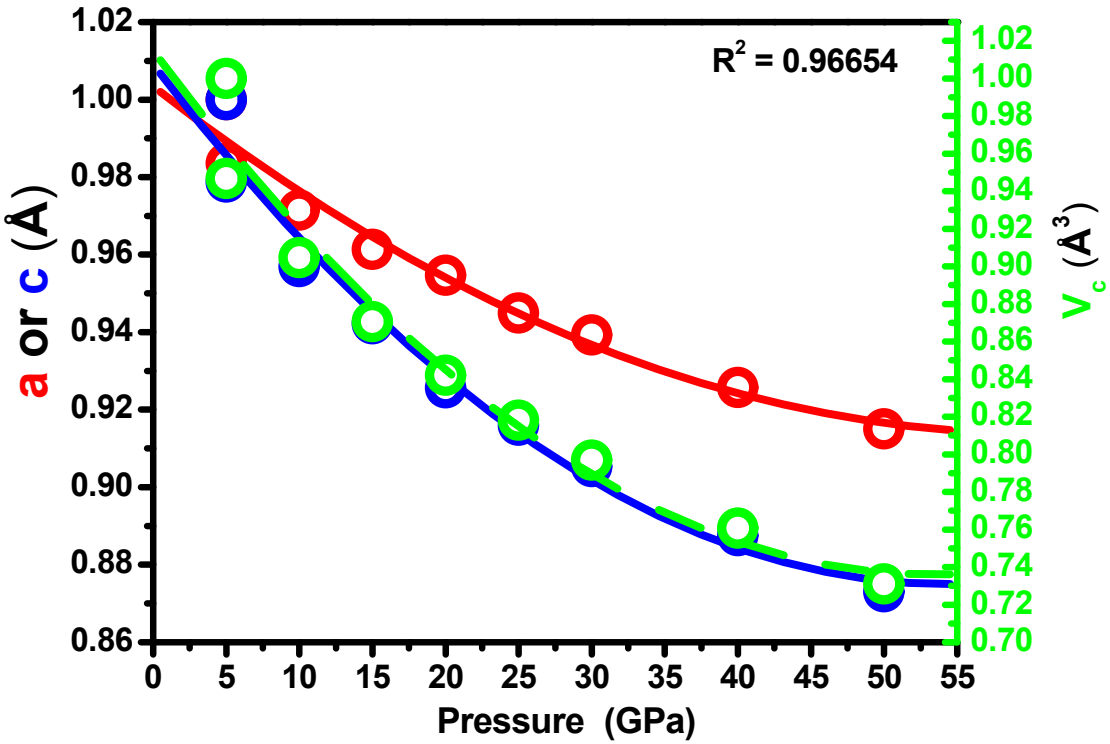

$B_0 = 81.80$ GPa with Computational parameters: cutoff 570 eV, **k**-point mesh optimization algorithm, and Harmon relativistic

Figure 4. Anisotropic structural compression of $MgAgF_3$ under hydrostatic pressure.

Normalized lattice parameters (a/a_0, c/c_0) and unit cell volume (V_c/V_0) as a function of pressure, where a_0, c_0, and V_0 are the ambient pressure values (see Table 1). Solid lines represent fits to the third-order Birch-Murnaghan equation of state. The volumetric fit yields a bulk modulus B_0 =

81.80 GPa with pressure derivative $B_0' = 3.90$. Fits to the individual lattice parameters reveal pronounced mechanical anisotropy: the linear bulk modulus along the a-axis ($B_{0,a} = 280.56$ GPa) is significantly higher than along the c-axis ($B_{0,c} = 185.51$ GPa), confirming the lower stiffness and higher compressibility parallel to the crystallographic c-direction.

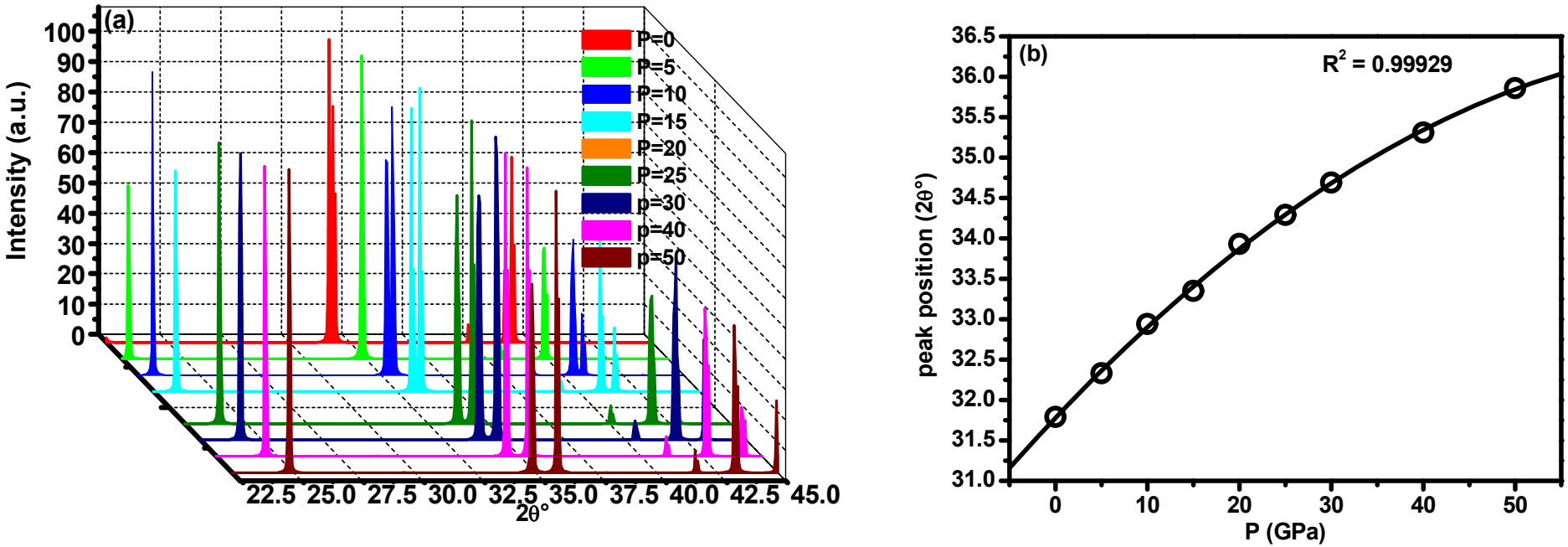

Figure 5. Pressure-dependent XRD patterns and peak evolution of $MgAgF_3$.

(a) A 3D simulated XRD patterns under hydrostatic pressure from 0 to 50 GPa. Patterns are normalized individually to their maximum intensity. With increasing pressure, all peaks systematically shift to higher 2θ angles. Above 10 GPa, characteristic peak splitting emerges, forming distinct doublet patterns between 15–30 GPa, which subsequently merge by 40 GPa. The doublet separation reaches a maximum of 0.083° at 15 GPa (Table 2). **(b)** Evolution of the strongest diffraction peak position (2θ) as a function of pressure. The peak shifts monotonically from 31.79° at

ambient pressure to 35.86° at 50 GPa, following a non-linear trend consistent with the material's compressibility. The data points correspond to the maximum intensity peak at each pressure: (1 1 0) at 0 GPa, (0 1 -4) at 5 GPa, (0 -1 4) at 10 GPa, (-1 1 4) at 15–20 GPa, (-1 0 -4) at 25 GPa, (-1 1 4) at 30–40 GPa, and (0 1 -4) at 50 GPa. The total shift of +4.07° corresponds to a *d*-spacing reduction of 11.1% over 50 GPa.

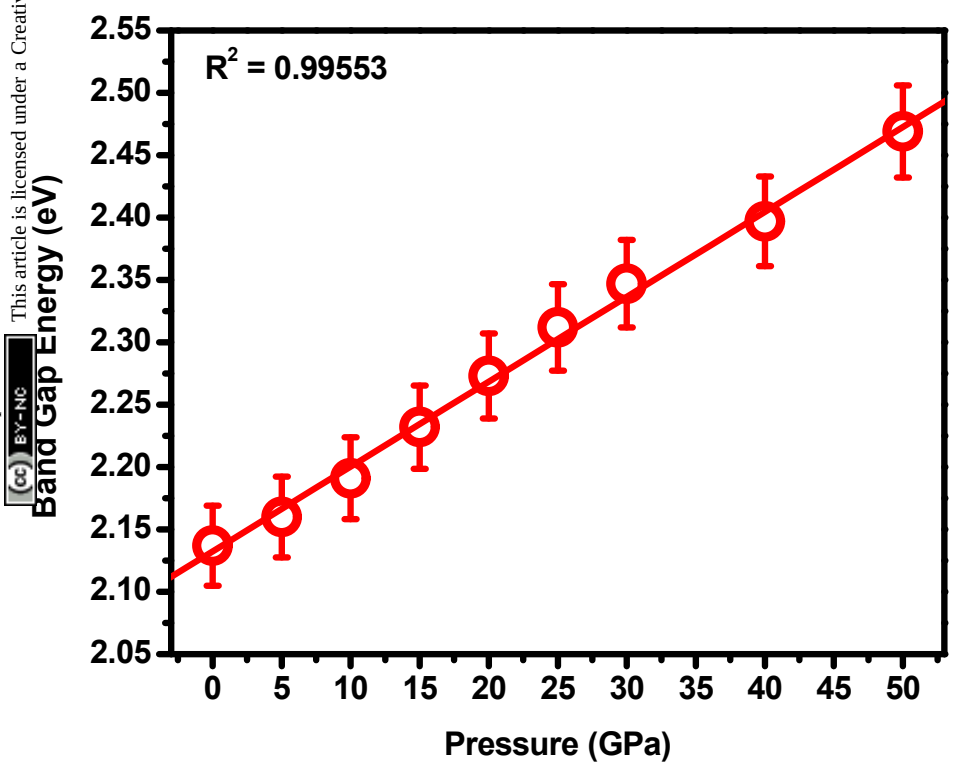

Figure 6. Pressure dependence of the electronic band gap of $MgAgF_3$.

Calculated band gap (PBE-GGA) of $MgAgF_3$ as a function of hydrostatic pressure from 0 to 50 GPa. The band gap increases linearly with pressure, following the relationship $E_g = 2.137 + 0.00667 \times P$ (eV), with $R^2 = 0.99553$ (solid line). The band gap increases from 2.137 eV at ambient pressure to 2.469 eV at 50 GPa, corresponding to an overall increase of 0.332 eV (15.5%). The band gap exhibits a smooth, continuous increase across the entire pressure range, with no discontinuities at the pressure regimes identified from the XRD analysis (Figure 5). This indicates that the pressure-induced structural changes do not alter the fundamental electronic character of the material, and the band gap widening is primarily driven by lattice compression and associated changes in bond lengths and orbital overlaps. The error bars represent the standard deviation of the band gap values obtained from the linear fit.

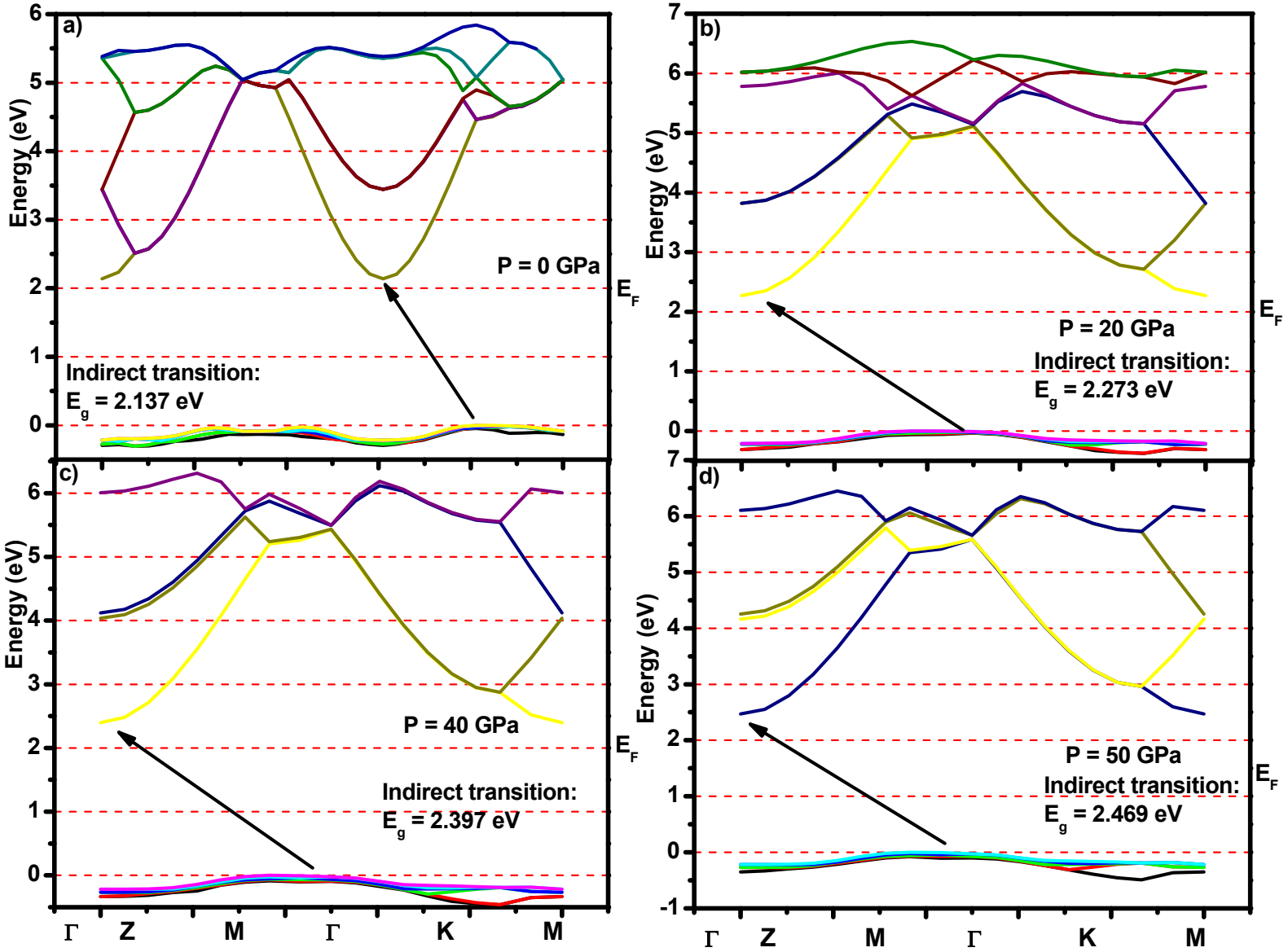

Figure 7. Band structure of $MgAgF_3$ under pressure.

Calculated band structures at **(a)** 0 GPa, **(b)** 20 GPa, **(c)** 40 GPa, and **(d)** 50 GPa are shown. The Fermi level (E_F) is set to 0 eV and indicated by the horizontal dashed line. Band structures are plotted along high-symmetry k-point paths in the hexagonal Brillouin zone ($\Gamma \rightarrow Z \rightarrow M \rightarrow \Gamma \rightarrow K \rightarrow M$). $MgAgF_3$ exhibits an indirect band gap at all pressures, with the valence band maximum at the Γ-point and the conduction band minimum along the Γ–Z direction. The band gap increases monotonically from 2.137 eV at 0 GPa to 2.469 eV at 50 GPa, consistent with the linear pressure dependence shown in Figure 6.

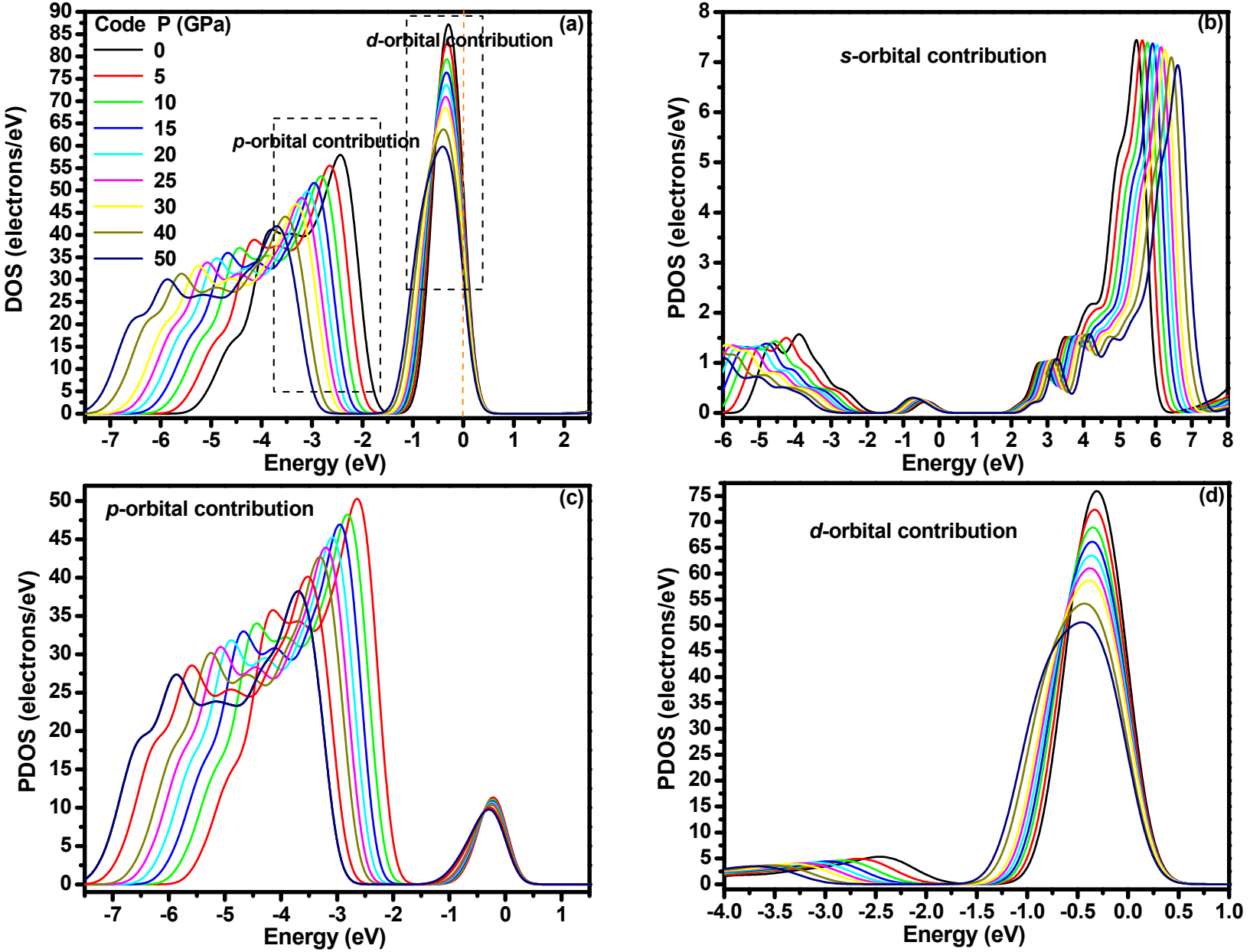

Figure 8. Pressure-dependent density of states and orbital-projected contributions in $MgAgF_3$.

(a) Total DOS. The energy gap widens monotonically with pressure from 2.137 eV to 2.469 eV (Figure 6), while the DOS broadens, reflecting enhanced orbital interactions under compression (Table 3, and Table 4). **(b) s-orbital contribution (s-PDOS).** s-states, originating primarily from F and Mg, dominate the lower valence band region and exhibit minimal pressure dependence. **(c) p-orbital contribution (p-PDOS).** p-states dominate both the valence band maximum (VBM) and conduction band minimum (CBM). F p-states contribute to the VBM, while Ag p-states contribute to the CBM. p-states broaden significantly with increasing pressure. **(d) d-orbital contribution (d-PDOS).** d-states originate exclusively from Ag, forming a narrow band centered near −0.5 eV at ambient pressure that broadens and shifts downward under compression. Increased Ag d–F p hybridization with pressure contributes to the widening band gap.

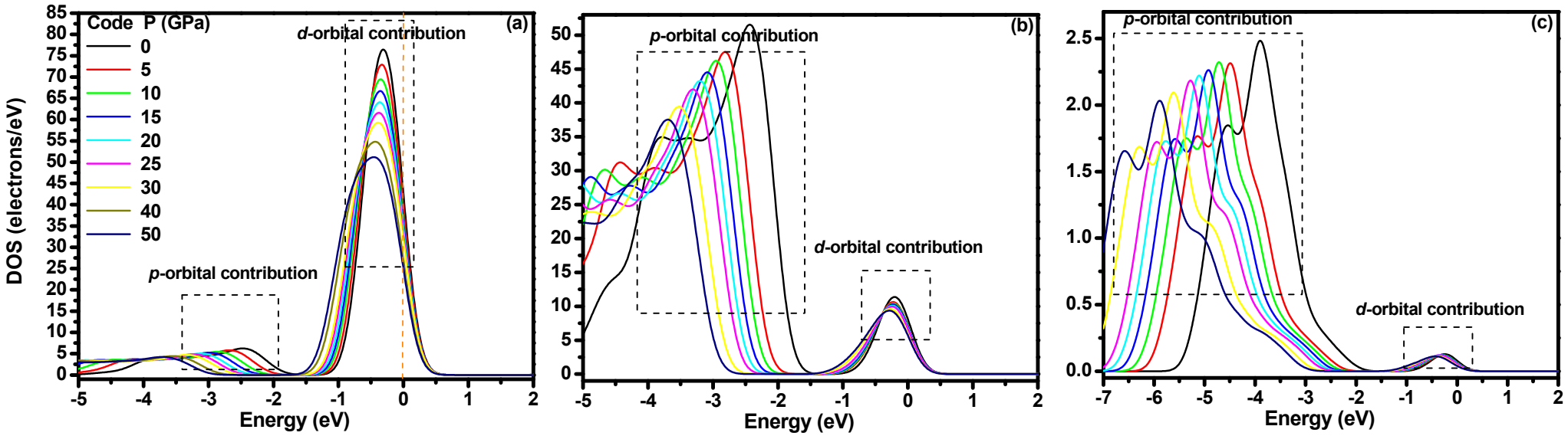

Figure 9. Atom-resolved partial density of states of $MgAgF_3$ under pressure.

Atom-projected PDOS for the Ag, F, and Mg atoms in the pressure range 0–50 GPa is shown. The Fermi level (E_F = 0 eV) is indicated by the vertical dashed line. **(a) Ag-atom:** Dominated by d-states forms a narrow band near −0.5 eV at ambient pressure. The d-band broadens and shifts downward under compression, indicating enhanced d–p hybridization. **(b) F-atom:** Dominated by p-states, which constitute the valence band maximum region. The p-band broadens systematically with pressure due to increased p–p orbital overlap. **(c) Mg-atom:** Under ambient conditions, Mg exhibits primarily s- and p-character. With increasing pressure, induced d-states emerge between −1 and 0 eV (just below the Fermi level), indicating pressure-induced hybridization between Mg and neighboring F and Ag atoms. These d-states broaden and intensify under compression, reflecting enhanced Mg–F covalent character consistent with the increasing bond overlap population (Table 3) and decreasing Mulliken charge (Table 4). All PDOS broaden with pressure, reflecting enhanced orbital interactions. The Ag d-band shows the most pronounced pressure response, while the band gap widens from 2.137 eV to 2.469 eV over 50 GPa.

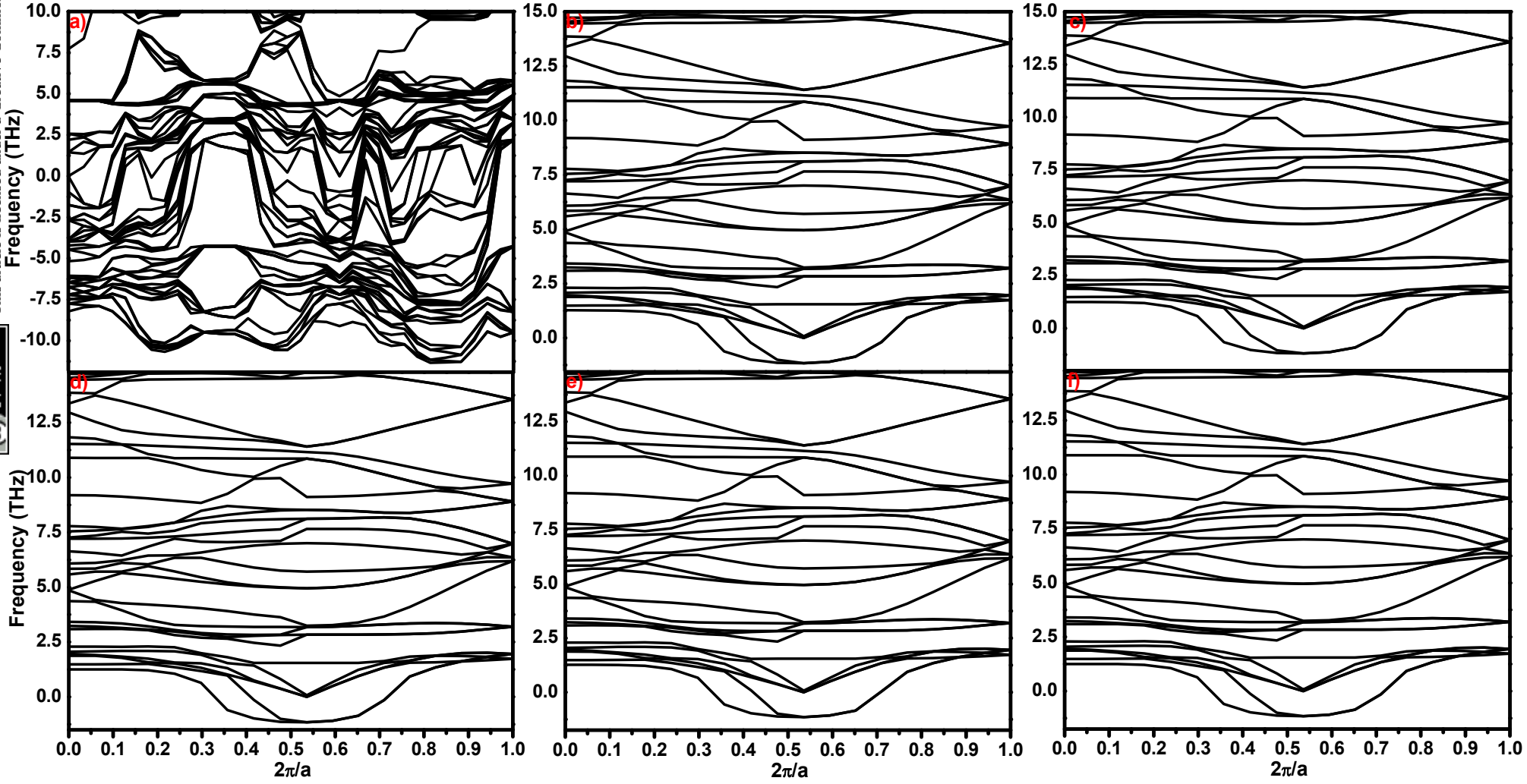

Figure 10. Pressure-dependent phonon dispersion of $MgAgF_3$.

Phonon dispersion curves along high-symmetry directions in the Brillouin zone at selected pressures: **(a)** 0 GPa, **(b)** 10 GPa, **(c)** 20 GPa, **(d)** 30 GPa, **(e)** 40 GPa, and **(f)** 50 GPa. Negative frequencies (imaginary modes) are plotted as negative values. At 0 GPa, significant imaginary frequencies (soft modes) are observed with a maximum magnitude of -11.3 cm^{-1}, indicating dynamical instability of the ambient structure. With increasing pressure, the magnitude of the soft modes decreases dramatically, reaching approximately -1.15 cm^{-1} at 10 GPa and remaining at this value up to 50 GPa. The persistence of small imaginary frequencies (≈ -1.15 cm^{-1}) across the 10–50 GPa range indicates that the high-pressure phase remains dynamically unstable, albeit with a very shallow potential well (see Table 5). The pressure-induced reduction in soft mode magnitude correlates with the XRD peak splitting and doublet formation observed at intermediate pressures (Figure 5), while the persistence of the weak instability suggests that the merging of XRD doublets at 40 GPa arises from a different mechanism, possibly a change in crystal symmetry.

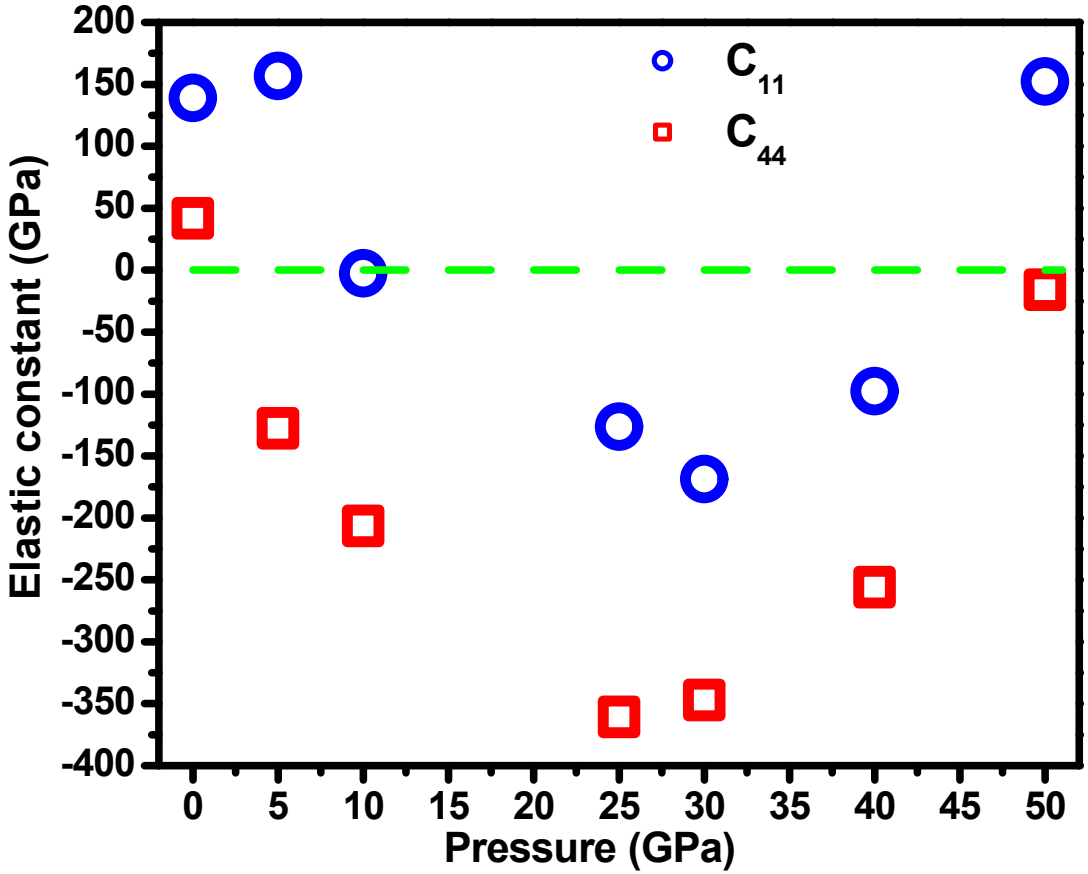

Figure 11. Pressure-dependent elastic constants C_{11} and C_{44} of $MgAgF_3$.

Axial stiffness C_{11} (blue circles) and shear constant C_{44} (red squares) as functions of hydrostatic pressure from 0 to 50 GPa. The horizontal dashed line at zero marks the Born stability threshold for trigonal crystals (positive values indicate mechanical stability). At 0 GPa, both constants are positive, confirming mechanical stability. C_{44} becomes negative at 5 GPa and remains negative throughout, while C_{11} becomes negative between 10–40 GPa and recovers to a positive value at 50 GPa.

Data Availability Statement

The datasets generated and/or analyzed during the current study are available from the corresponding author upon reasonable request. All relevant computational input files, raw data, and processed results will be shared with editors or reviewers if required for verification purposes.